UNIVERSITÀ DEGLI STUDI DI ROMA
“TOR VERGATA”

Facoltà di Ingegneria

Corso di Laurea in Ingegneria Meccanica

Tesi di Laurea Magistrale in Ingegneria Meccanica

DLR-F6 design optimization by means of Radial Basis Functions mesh morphing

Thesis supervisor	Candidate
Eng. Marco Evangelos Biancolini	**Marco Gozzi**
Industrial supervisor	Assistant supervisor
PhD Eng. Emiliano Costa	**PhD Eng. Corrado Groth**

Anno Accademico 2012/2013

To my parents,
Gabriella e Maurizio.

CONTENTS

INTRODUCTION

Aerodynamic design and development of civil and military aircraft relies to an increasing extent on *Computational Fluid Dynamics (CFD)* analysis tools as time goes on. Aircraft design optimization driven by a CFD study combined with mesh morphing allows to improve aircraft performances in a reasonable time.

The design process starts with the intended purpose of the aircraft. Commercial airliners require greater efficiency in order to reduce fuel consumption because they need a long range of flight. An increase in the number of aircraft also means greater carbon emissions. Moreover performances could be demanded depending on the mission of the airplane.

The aim of this work is to provide a suitable method for aircraft design optimization by means of radial basis function (RBFs). The suggested workflow can be applied to a wide range of fluid dynamics studies where a shape optimization is needed.

In the present work a wing shape optimization of the model referred to as *DLR-F6* has been accomplished combining eight *shape parameters* of the wing and nacelle (engine housing cover) that are dihedral angle, sweep angles, twist of the wing and two rigid translations and one rotation of the nacelle.

The range of variation of each parameter has been evaluated taking under consideration what its modification could induce to aircraft stability, manoeuvrability and safety.

The process consisted, at first, in calculating with *ANSYS Fluent* the reference values of *Lift*, *Drag* and their related coefficients (Cd, Cl, Cm) of the aircraft model. Later, the above mentioned values have been compared with the corresponding ones performed at French Aerospace Centre (*ONERA*) facility. Then mesh morphing has been applied to two kind of meshes (a coarse mesh with 3 million of cells and a fine mesh with 14 million of cells) using the commercial morpher RBF-Morph; in this way, parametric meshes have been generated so as to be analysed with a design of experiments (DOE) in order to identify the best configuration of the aircraft in cruise conditions. The whole procedure of computation has been automated using *ANSYS Workbench.*

In first chapter, theory of *Computational Fluid Dynamics* will be discussed and turbulence model, used in this work, will be presented.
The second chapter concerns flight dynamics, forces and coefficients commonly used in aeronautics, whereas in the chapter three, DLR-F6 geometry will be presented with a discussion about aircraft parameters which will be changed during the workflow.
RBF theory and the *ANSYS Fluent* add-on *RBF-Morph* will be treated in the fourth chapter.
Finally, chapter five and six are about simulations and results. In these two sections the whole workflow will be discussed including DOE and a fine configuration of the aircraft will be shown.

1 CFD

CFD is the analysis of systems involving fluid flow, heat transfer and associated phenomena such as chemical reactions by means of computer-based simulation. The technique is very powerful and spans a wide range of industrial and non-industrial application areas.

From the 1960s onwards the aerospace industry has integrated CFD techniques into the design, R&D and manufacture of aircraft and jet engines. More recently the methods have been applied to the design of internal combustion engines, combustion chambers of gas turbines and furnaces. Furthermore, motor vehicle manufacturers now routinely predict drag forces, under-bonnet air flows and the in-car environment with CFD. Increasingly CFD is becoming a vital component in the design of industrial products and processes.

The ultimate aim of developments in the CFD field is to provide a capability comparable to other CAE (Computer-Aided Engineering) tools such as stress analysis codes. The main reason why CFD has lagged behind is the tremendous complexity of the underlying behaviour, which precludes a description of fluid flows that is at the same time economical and sufficiently complete. The availability of affordable high performance computing hardware and the introduction of user-friendly interfaces have led to an upsurge of interest and CFD is poised to make an entry into the wider industrial community since the 1990s.

The governing equations of fluid flow are Navier-Stokes equations; they represent mathematical statements of the conservation laws of physics: mass conservation, momentum, rotational momentum and energy.

CFD can solve Navier-Stokes equations using closed form expression for laminar flows (low Reynolds numbers) and simple geometries, and using numerical methods for turbulent flows and complex geometries.

CFD codes are structured around the numerical algorithms that can tackle fluid flow problems. In order to provide easy access to their solving power, all commercial CFD packages include sophisticated user interfaces to input problem parameters and to examine the results.

The most used method is the finite volume method and it was originally developed as a special finite difference formulation. Values are calculated at discrete places on a meshed geometry. "Finite volume" refers to the small volume surrounding each node point on a mesh. In the finite volume method, volume integrals in a partial differential equation that contain a divergence term are converted to surface integrals, using the divergence theorem. These terms are then evaluated as fluxes at the surfaces of each finite volume. Because the flux entering a given volume is identical to that leaving the adjacent volume, this method is conservative.

The numerical algorithm consists of the following steps:

- Formal integration of the governing equations of fluid flow over all the (finite) control volumes of the solution domain.
- Discretisation involves the substitution of a variety of finite-difference-type approximations for the terms in the integrated equation representing flow processes such as convection, diffusion and sources. This converts the integral equations into a system of algebraic equations.
- Solution of the algebraic equations by an iterative method.

1.1 Governing equations of fluid flow

The governing equations of fluid flow represent mathematical statements of the conservation laws of physics.

- The mass of a fluid is conserved.
- The rate of change of momentum equals the sum of the forces on a fluid particle (Newton's second law).
- The rate of change of energy is equal to the sum of the rate of heat and the rate of work done on a fluid particle (first law of thermodynamics).

The flux can be in general decomposed into two different parts: one due to the convective transport and the other one due to the molecular motion present in the fluid at rest. This second contribution is of a diffusive nature and it is proportional to the gradient of the quantity considered and hence it will vanish for a homogeneous distribution.

In the study of continua (fluids, in particular) we will not be interested in the properties of each molecule such as velocity, pressure, density and temperature at a certain point but in the average of these properties over a large number of molecules in the vicinity of the respective point (molecule).

1.1.1 The continuity equation

This principle can be formulated considering a control volume V_0 bounded by a surface S_0.

The law of mass conservation expresses the fact that mass cannot be created in such a fluid system, nor can disappear from it.

$$\frac{\partial}{\partial t}\int_{V_0} \rho \, dV + \oint_{S_0} \rho \vec{u} * \hat{n} \, dS = 0 \qquad 1.1$$

Where:

ρ is the fluid density
$\vec{u}$ velocity
$\hat{n}$ normal to the surface S

Equation 1.1 expresses the mass conservation using integrals. If the fluid flow is in a steady state we can eliminate the first term and write the second one in another way. Using the divergence theorem the 1.1 can be expressed in a differential form.

$$\frac{\partial \rho}{\partial t} + \vec{\nabla}(\rho \vec{u}) = 0 \qquad 1.2$$

1.1.2 The momentum equation

Newton's second law states that the rate of change of momentum of a fluid particle equals the sum of the forces on the particle. The mathematical expression is:

$$\frac{\partial}{\partial t}\int_{V_0} \rho \vec{u}\, dV + \oint_{S_0} \rho\, \vec{u}(\vec{u} * \hat{n}) dS + \oint_{S_0} p\hat{n}\, dS = \vec{F}_S + \vec{F}_V \qquad 1.3$$

Where **F**$_S$ are the surface forces which act directly on the surface of the control volume such as pressure forces and viscous forces (shear and normal stresses); **F**$_V$ are the volume or body forces which act directly on the mass of the volume. These are for example gravitational, buoyancy, Coriolis or centrifugal forces. In some cases, there can be electromagnetic forces present as well.

1.1.3 The energy equation

The first law of thermodynamics, applied to the control volume, states that any changes in time of the total energy inside the volume are caused by the rate of work $\dot{L}$ of forces acting on the volume and by the net heat flux $\dot{Q}$ into it.

$$\frac{dE}{dt} = \dot{L} + \dot{Q} \qquad 1.4$$

If we call ε the energy per unit mass, we can write the following formula:

$$\frac{\partial}{\partial t}\int_{V_0} \rho \varepsilon dV + \int_{S_0} \rho \varepsilon \vec{u} * \hat{n} dS = \dot{L} + \dot{Q} \qquad 1.5$$

1.2 Turbulence models

In 1937, Taylor and Von Karman proposed the following definition of turbulence: "*Turbulence is an irregular motion which in general makes its appearance in fluids, gaseous or liquid, when they flow past solid surfaces or even when neighboring streams of the same fluid flow past or over one another.*"

The basic phenomenology of turbulence can be recovered from a simple dimensional analysis of Navier-Stokes equations, using the image of the *turbulent cascade*.

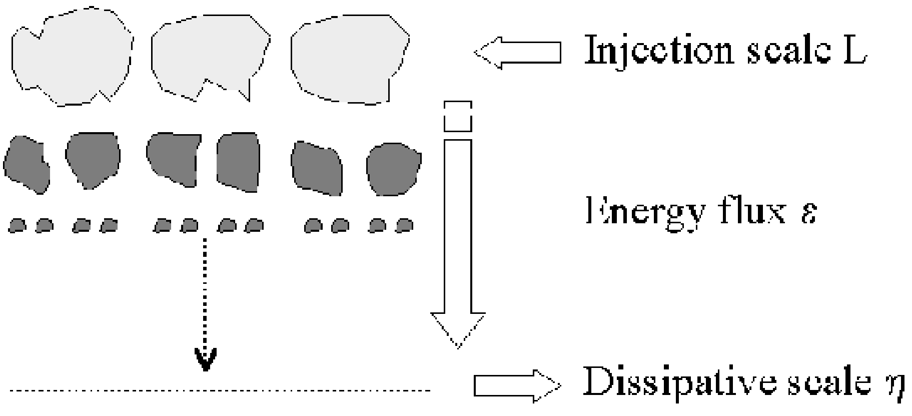

Figure 1.1 – Turbulent cascade

The kinetic energy is supposed to be injected by an external forcing which sustains the motion of large scale eddies. This structures are deformed and stretched by the fluid dynamics, until they break into smaller eddies, and the process is repeated such that energy is transported to smaller and smaller structures. Finally at small scales (Kolmogorov scales η[1]) the kinetic energy is dissipated by the viscosity of the fluid. The whole process of transport of energy from the large scale of injection to the small dissipative scale, through the hierarchy of eddies is known as turbulent cascade.

Virtually, all flows of practical engineering interest are turbulent. Turbulent flows always occur when the Reynolds number is large. Careful analysis of solutions to the Navier-Stokes equation, or more typically to its boundary-layer form, show that turbulence develops as an instability of laminar flow. For high Reynolds number, the energy cascade can be very large and so, if we would capture all of the significant structures of the turbulence, the domain on which the computation is performed should be at least as large as the physical domain to be considered. A valid simulation must also capture all of the kinetic energy dissipation. This occurs on the smallest scales, the ones on which viscosity is active, so the size of the grid must be no larger than a viscously determined scale, called the Kolmogoroff scale. Since the number of grid points that can be used in a computation is limited by the processing speed and memory of the machine on which it is carried out, *DNS (Direct Numerical Simulation)* is possible only for flows at relatively low Reynolds numbers and in geometrically simple domains.

Alternative methods consist in modeling turbulence “cutting” the length scale at a certain point in order to predict the flow behaviour. For most engineering applications it is unnecessary to resolve the details of the turbulent fluctuations. Turbulence models allow the calculation of the mean flow without first calculating the full time-dependent flow field.

The most used methods are the Reynolds-averaged approaches (*RANS, Reynolds Averaged Navier-Stokes Equations*) and consist in considering each

---

[1] $\eta=(\nu^3/\varepsilon)^{1/4}$ is the length of Kolmogorov scale where ν is kinematic viscosity and ε is the dissipated energy per unit mass

variable composed by a mean (time averaged) value $\bar{b}$ and a fluctuating component b'.

$$\boldsymbol{b = \bar{b} + b'} \qquad 1.6$$

The time averaged variable b is:

$$\boldsymbol{\bar{b} = \frac{1}{\Delta t}\int_{t_0}^{t_0+\Delta t} b\, dt}. \qquad 1.7$$

Moreover if Δt is enough long, the average value of the fluctuating component b', $\overline{b'} = \int_{t_0}^{t_0+\Delta t} b'\, dt,$ is zero.

Using these statements in the Navier Stokes equations we can write:

$$\boldsymbol{\frac{\partial \bar{u}_i}{\partial x_i} = 0} \qquad 1.8$$

$$\boldsymbol{\bar{u}_i \frac{\partial \bar{u}_j}{\partial x_i} = -\frac{1}{\rho}\frac{\partial \bar{p}}{\partial x_j} + \nu \frac{\partial^2 \bar{u}_i}{\partial x_i^2} - \frac{\partial \overline{u'_j u'_i}}{\partial x_i}} \qquad 1.9$$

The presence of the Reynolds stresses and turbulent scalar flux in the conservation equations means that the latter are not closed, that is to say, they contain more variables than there are equations. Closure requires use of some approximations, which usually take the form of prescribing the Reynolds stress tensor 1.10 and turbulent scalar fluxes in terms of the mean quantities.

$$\mathrm{r_{ij}} = \boldsymbol{-\overline{u'_i u'_j}} \qquad 1.10$$

To close the equations we must introduce a turbulence model using the Boussinesq's hypothesis:

$$\boldsymbol{r_{ij} = -2\nu_t s_{ij}} \qquad 1.11$$

Where

$$\boldsymbol{s_{ij} = \frac{1}{2}\left(\frac{\partial \bar{u}_i}{\partial x_j} + \frac{\partial \bar{u}_j}{\partial x_i}\right)} \qquad 1.12$$

The hypothesis relates the turbulence stresses to the mean flow by analogy with the viscous stress tensor and the deformation rate.

In the following paragraph the *Spalart-Allmaras* model will be discussed since this method has been used in the present study.

1.2.1 Spalart-Allmaras model

The *Spalart-Allmaras* model is called *one equation model*. It solves a transport equation for a viscosity-like variable $\tilde{\nu}$.

It includes eight closure coefficients and three damping functions. Its defining equations are as follows:

Eddy Viscosity Equation

$$\frac{\partial \tilde{\nu}}{\partial t} + u_j \frac{\partial \tilde{\nu}}{\partial x_j} = c_{b1}(1 - f_{t2})\bar{S}\tilde{\nu} - \left[c_{w1} f_w - \frac{c_{b1}}{k^2} f_{t2}\right]\left(\frac{\tilde{\nu}}{d}\right)^2 + \frac{1}{\sigma}\left[\frac{\partial}{\partial x_j}\left((\nu + \tilde{\nu})\frac{\partial \tilde{\nu}}{\partial x_j}\right) + c_{b2}\frac{\partial \tilde{\nu}}{\partial x_i}\frac{\partial \tilde{\nu}}{\partial x_i}\right] + f_{t1}(\Delta q)^2 \qquad 1.13$$

Kinematic Eddy Viscosity $\nu_t = \tilde{\nu} f_{v1}$

With

$$f_{v1} = \frac{\chi^3}{\chi^3 + c_{v1}^3}$$

and $\chi = \frac{\tilde{\nu}}{\nu}$ where ν=μ/ρ is the kinematic viscosity.

$$\bar{S} = S + \frac{\tilde{\nu}}{k^2 d^2} f_{v2}$$

where

- d is the distance from the wall
- k is the von Karman costant
- S is the modulus of the vorticity vector $\vec{\xi}$

with

$$\vec{\xi} = \left(\frac{\partial W}{\partial y} - \frac{\partial V}{\partial z}\right)\vec{\imath} + \left(\frac{\partial U}{\partial z} - \frac{\partial W}{\partial x}\right)\vec{\jmath} + (\frac{\partial V}{\partial x} - \frac{\partial U}{\partial y})\vec{k}$$

and

$$f_{v2} = 1 - \frac{\chi}{1 + \chi f_{v1}}$$

f_w is defined by:

$$f_w(r) = g(\frac{1 + c_w^6}{g^6 + c_w^6})^{1/6}$$

Where

$$g = r + c_{w2}(r^6 - r)$$

and

$$r = \min[\frac{\tilde{\nu}}{Skd^2}; 10]$$

f_{t1} is given by:

$$f_{t1} = c_{t1} g_t \exp[-c_{t2}\left(\frac{\omega_t}{\Delta q}\right)^2 (d^2 + g_t^2 d_t^2)]$$

and f_{t2} by:

$$f_{t2} = c_{t3}\exp(-c_{t4}\chi^4)$$

Other costants are:

- $\sigma = 2/3$
- $c_{b1}=0.1355$
- $c_{b2}=0.622$
- $k=0.41$
- $c_{v1}=0.71$
- $c_{w2}=0.3$
- $c_{w3}=2$
- $c_{t1}=1$
- $c_{t2}=2$

- c_{t3}=1.1
- c_{t4}=2

Finally, boundary conditions are:

- Inlet section $\tilde{\nu} = \nu_\infty$
- Wall: $\tilde{\nu} = 0$
- Far field: $0 < \tilde{\nu} \leq 1/10\ \nu_\infty$

2 FLIGHT DYNAMICS AND PHYSICS

In this chapter a brief introduction on flight dynamics will be presented. The terms governing the physics of the airfoil are defined below.

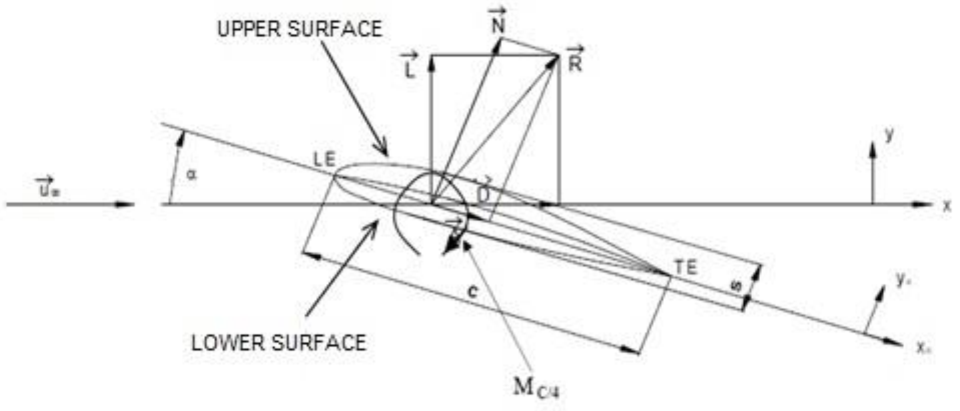

Figure 2.1 – Airfoil with related acting forces

Where:

c = chord line
LE = leading edge
TE = trailing edge
s = thickness
α = angle of attack
$\vec{u}_\infty$ = undisturbed flow speed

An airfoil-shaped body moved through a fluid produces an aerodynamic force. The component of this force perpendicular to the direction of motion is called lift. The component parallel to the direction of motion is called drag. Subsonic flight airfoils have a characteristic shape with a rounded leading edge, followed by a sharp trailing edge, often with asymmetric camber. The lift on an airfoil is primarily the result of its angle of attack and shape. When oriented at a suitable angle, the airfoil deflects the oncoming air, resulting in a force on the airfoil in the direction opposite to the deflection.

In order to better define an aircraft wing we have to mention other parameters which descibe the wing planform because this feature very affects the lift distribution.

The *wingspan b* of an aircraft is always measured in a straight line, from wingroot to wingtip, independently of wing shape or sweep.

The *aspect ratio* of a wing is essentially the ratio of its length b to its breadth (mean chord c). It's also defined as the square of the wingspan b divided by the area S of the wing planform. A high aspect ratio indicates long, narrow wings, whereas a low aspect ratio indicates short, stubby wings.

$$\boldsymbol{A = \frac{b^2}{S} = \frac{b}{c}} \tag{2.1}$$

The *taper ratio* λ is the ratio of the chord tip c_t to the chord root c_r.

$$\boldsymbol{\lambda = \frac{c_t}{c_r}} \tag{2.2}$$

The above mentioned parameters will not be varied in this study because the DLR-F6 has a clear-cut geometry; other features that will be customized will be deeply described in chapter 3.

2.1 Aerodynamic forces

When an aircraft flies through the air some forces act on the object and they can be taken into account using principles of aerodynamics. The fluid flow generates a force F on the airplane surfaces S which has modulus and direction depending on the flight conditions. F is due to normal pressure p and shear stresses τ caused by the interaction between air flow and surfaces.

$$\boldsymbol{F = \int_S (-p\,\hat{n} + \tau\,\hat{t})\,dS} \tag{2.3}$$

Where $\hat{n}$ and $\hat{t}$ are the unit vectors normal and tangential to the aircraft surface.

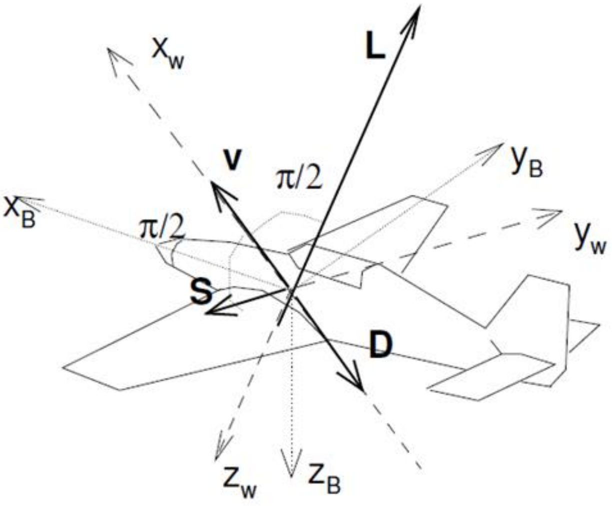

Figure 2.2 – Acting forces on airplane

Another way to express F is:

$$\boldsymbol{F} = \frac{1}{2}\boldsymbol{\rho V^2 S C_f} \qquad 2.4$$

And it can be represented by three components among the axes (x_B, y_B, z_B):

$$\boldsymbol{F} = -\begin{bmatrix} \boldsymbol{D} \\ \boldsymbol{S} \\ \boldsymbol{L} \end{bmatrix} = -\frac{1}{2}\boldsymbol{\rho V^2 S}\begin{bmatrix} \boldsymbol{C_D} \\ \boldsymbol{C_S} \\ \boldsymbol{C_L} \end{bmatrix} \qquad 2.5$$

Where ρ is the density of the fluid, S the cross-sectional area, V is the speed modulus of the object relative to the fluid and C_f is a vector which components are the aerodynamic coefficients. These coefficients are C_D, C_L and C_S and they depend on the speed, Reynolds number and Mach number. Lift (L) and drag (D) have both two a large effect to the performance of the plane. The aerodynamic resistance is parallel and opposite to the free-stream direction V and it is mainly a dissipative force so the aircraft needs a forward thrust sistem to fly. Lift is perpendicular to the flow direction then it doesn’t do work.

Types of drag are generally divided into the following categories:

- parasitic drag, consisting of
    - form drag,
    - skin friction,
    - interference drag,
- lift-induced drag
- wave drag.

The phrase parasitic drag is mainly used in aerodynamics, since for lifting wings drag is in general small compared to lift. For flow around bluff bodies, drag is most often dominating, and then the qualifier "parasitic" is meaningless. Form drag, skin friction and interference drag on bluff bodies are not coined as being elements of "parasitic drag", but directly as elements of drag. Further, lift-induced drag is only relevant when wings or a lifting body are present, and it is therefore usually discussed either in the aviation perspective of drag, or in the design of either semi-planing or planing hulls. Wave drag occurs when a solid object is moving through a fluid at or near the speed of sound in that fluid.

2.2 Aerodynamic coefficients

Once the aerodynamic forces are defined it is possible to characterize the relative coefficients:

$$c_l = \frac{L}{\frac{1}{2}\rho_\infty U_\infty^2 S} \qquad c_d = \frac{D}{\frac{1}{2}\rho_\infty U_\infty^2 S} \qquad c_m = \frac{M}{\frac{1}{2}\rho_\infty U_\infty^2 c\, S} \qquad 2.6$$

These parameters are very useful to evaluate the airplane efficiency and to determine the finest configuration. It is common to show, for a particular airfoil section, the relationship between section lift coefficient and angle of attack as represented by the formula 2.7.

If the airfoil is enough thin, $c_{l\alpha} \approx 2\pi$ and it doesn't depend on the airfoil camber and thickness; α_0 is the angle of attack corresponding to the zero lift condition.

$$\boldsymbol{c_l = c_{l\alpha}(\alpha - \alpha_0)} \qquad \mathbf{2.7}$$

The angle at which maximum lift coefficient $C_{l\ max}$ occurs is the stall angle of the airfoil, over this value the lift coefficient decreases as depicted in figure 2.3. The lift coefficient is strictly affected by several factors: $c_l = f(\alpha, Re, M, shape)$

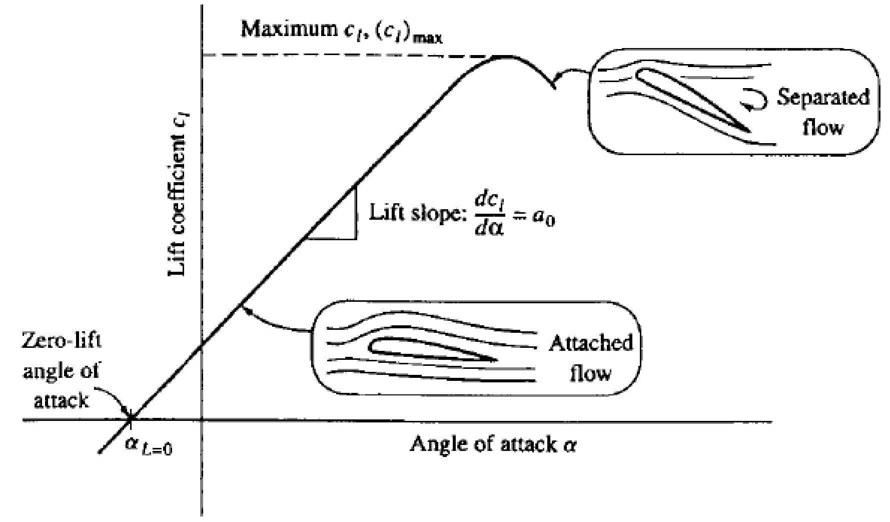

Figure 2.3 – Lift coefficient vs. angle of attack

In a similar way the Cd trend is shown in Figure 2.4. Drag coefficient increases in a non linear way with the angle of attack and it's affected by the same factors: $c_d = f(\alpha, Re, M, shape)$.

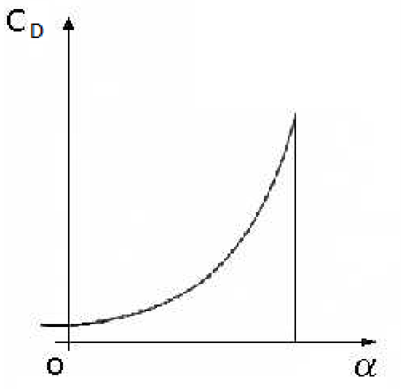

Figure 2.4 - Drag coefficient vs. angle of attack

The relationship between lift and drag is the *efficiency* and it is also called lift-to-drag ratio and it is represented by the polar plot:

$$E = \frac{c_l}{c_d} \tag{2.8}$$

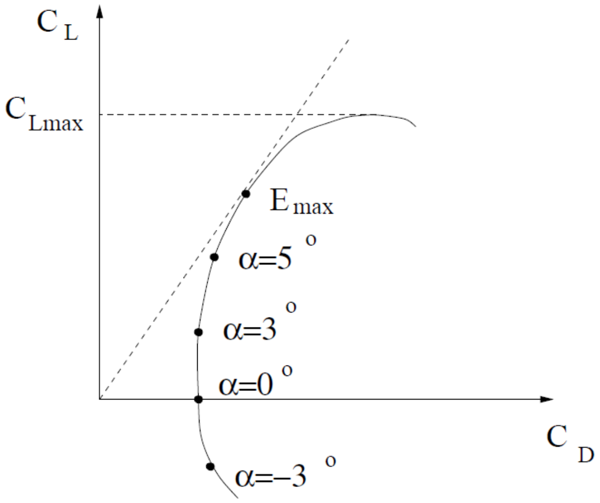

Figure 2.5 – Polar plot

Efficiency is useful to choose the best aifoil, it is possible to find the maximum value drawing a tangent line to the polar drag passing through the origin.

Pressure coefficient is another important coefficient in aerodynamics which describes the relative pressures throughout a flow field.

$$c_p(x) = \frac{p(x) - p_\infty}{\frac{1}{2}\rho U_\infty^2} \qquad 2.9$$

Where the terms with ∞ are referred to freestream conditions and x refers to the point at wich the pressure is being evaluated. In the fluid flow field around a body there will be points having positive pressure coefficients up to one, and negative pressure coefficients including coefficients less than minus one, but nowhere will the coefficient exceed plus one because the highest pressure that can be achieved is the stagnation pressure.

On the upper surface of the airfoil the pressure is less than the freestream pressure $p<p_\infty$ so the $C_p<0$, whereas in the lower surface $p>p_\infty$ and $C_p>0$. The point P is the stagnation point where the pressure is the stagnation pressure, the speed is equal to zero and $C_p=1$[2].

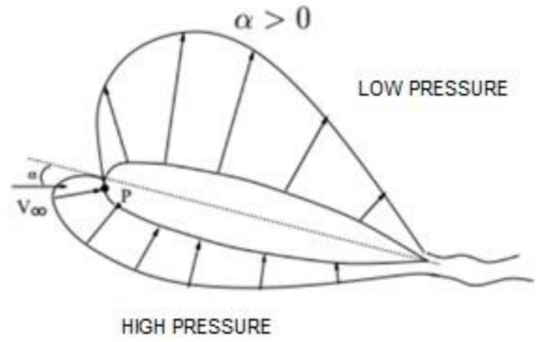

Figure 2.6 – Pressure distribution on airfoil

A tipical coefficient pressure distrubution on an airfoil is shown in Figure 2.7, as you can see, a graph of this distribution is drawn so that negative numbers are higher on the graph. The coefficient of lift for an airfoil can be calculated from the coefficient of pressure distribution calculating the area between the lines on the distribution.

---

[2] Cp value can be higher than one for compressible flows

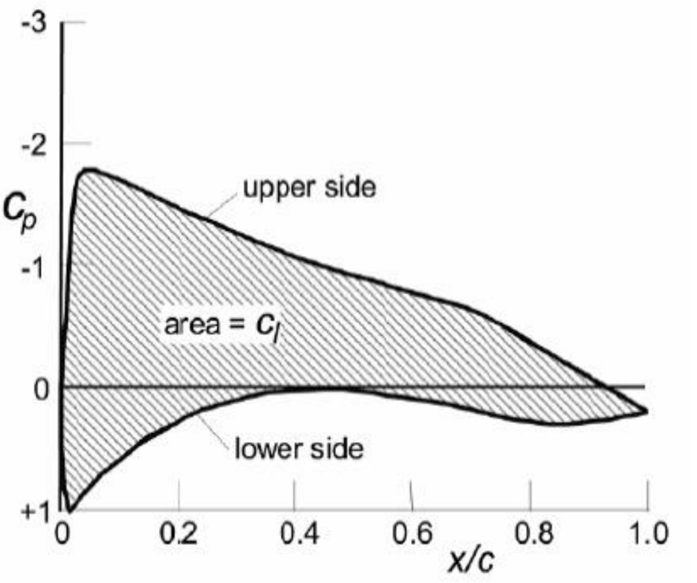

Figure 2.7 – Cp distribution on airfoil

2.3 Compressibility

As an aircraft moves through the air, the air molecules near the aircraft are disturbed and move around the aircraft. If the aircraft passes at a low speed the density of the air remains constant. But for higher speeds, some of the energy of the aircraft goes into compressing the air and locally changing the density of the air. This compressibility effect alters the amount of resulting force on the aircraft. The effect becomes more important as speed increases. Even though the speed of the airplane is less than the speed sound, in some surface points sound speed can be reached and exceeded. In this work, Mach number is set to 0.75, as proposed by Nasa in the *2° Drag Prediction Workshop* for cruise conditions, so we can assume that aircraft flies in subsonic condition just below transonic field.

3 DLR-F6 MODEL

Since 2001, several case studies were proposed by AIAA (*American Institute of Aeronautics and Astronautics*) in order to involve a large number of aeronautical experts. These kind of studies were called Drag Prediction Workshop (DPW).

The objectives were the follows:

- To assess the state-of-the-art computational methods as practical aerodynamic tools for aircraft force and moment prediction of increasingly complex geometries.
- To provide an impartial forum for evaluating the effectiveness of existing computer codes and modelling techniques using Navier-Stokes solvers.
- To identify areas needing additional research and development.

From 2001 to 2012, 5 *Workshops* were proposed. The present work deals with the second *Workshop* then only the first and the second *D.P.W.* will be discussed.

The aircraft model is the DLR-F6 and consists in a fuselage, wing, nacelle and pylon (WBNP). This model represents a typical passengers aircraft and it's useful for wind tunnel testing, in fact several experiments were accomplished by the most important aerospace research centres in Europe, such as *ONERA* in France, *NLR* in Holland, *DLRA* in Germany and *RAE* in England.
The wind tunnel tests were used for C.F.D validation.

3.1 AIAA Drag Prediction Workshop

3.1.1 Workshop 1

The first Workshop concerns DLR-F4 model which is previous than DLR-F6 and it doesn't have nacelle and pylon. The geometry used for DLR-F4 is shown in Figure 3.1 whereas in Figure 3.2 the DLR-F4 airfoil is depicted.

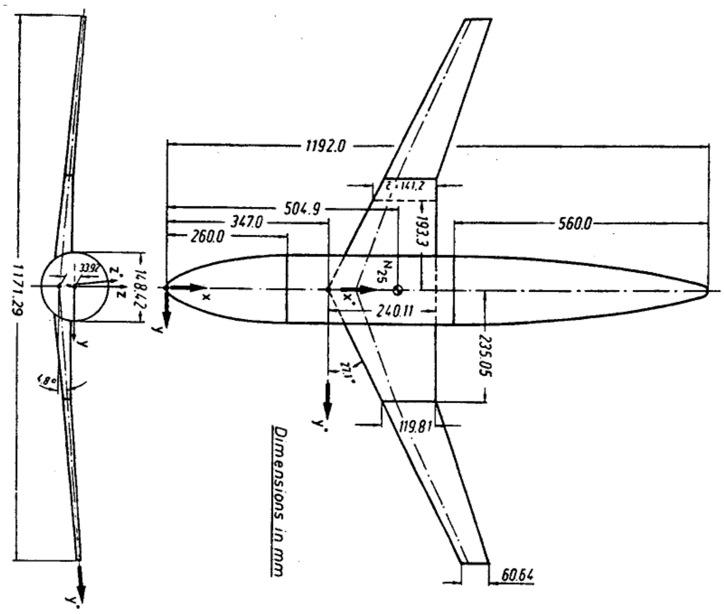

Figure 3.1 – DLR-F6 geometry

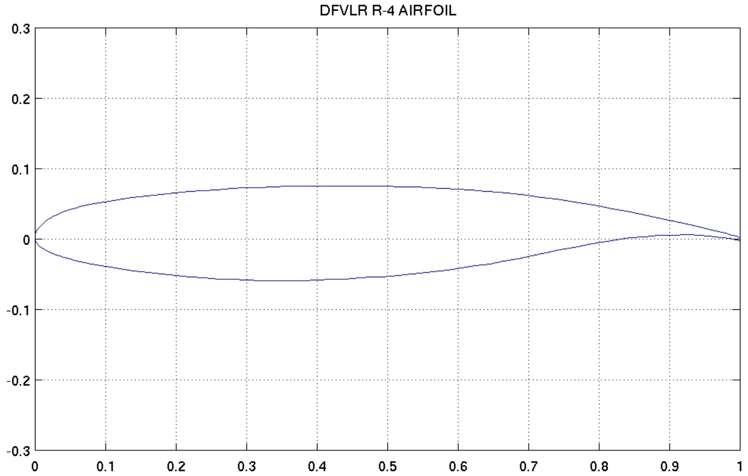

Figure 3.2 – DLR-F4 airfoil

The problem was proposed by *NASA* with the following settings:

- Re = 3*10^6
- Mach number = 0.75
- $C_L = 0.500 \pm 0.001$
- Angle of attack α = -3°, -2°, -1°, 0°, 1°, 2°; (1 degree for cruise conditions)

3.1.2 Workshop 2

The second workshop leads to the study of DLR-F6, this new configuration is different from the DLR-F4 because is characterized by a better and elliptical lift distribution. The difference between F6 and F4 is shown in Figure 3.3.

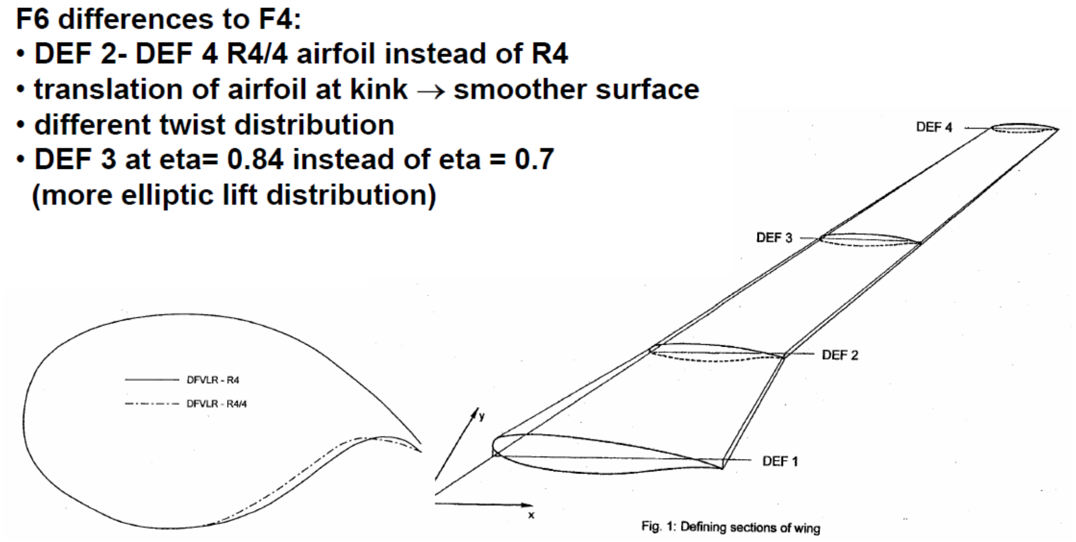

F6 differences to F4:
- **DEF 2- DEF 4 R4/4 airfoil instead of R4**
- **translation of airfoil at kink → smoother surface**
- **different twist distribution**
- **DEF 3 at eta= 0.84 instead of eta = 0.7 (more elliptic lift distribution)**

Figure 3.3 – Differences between DLR-F6 and DLR-F4

- Re = 3*10^6
- T = 305 K
- Mach number = 0.75 (cruise conditions)
- Angle of attack α = -3°, -2°, -1°, 0°, 1°, 1.5° (1 degree for cruise conditions)
- $C_L = 0.5 \pm 0.001$

More details about parameters and aircraft performances will be explained in the following section.

3.2 DLR-f6 geometry

A brief description of the parameters that will be implemented on DLR-f6 *(Drag Prediction Worksoph II)* is presented in the following section.

A range of each parameter is proposed taking under consideration the following observation:

- The aim of this research is to minimize *Drag,* improve *Lift* and *Lift*-to-*Drag* ratio *(Efficiency).*
- The modification of parameters could affect aircraft stability, manoeuvrability and safety.

Following graphs show aerodynamic coefficients related to the wind tunnel model.

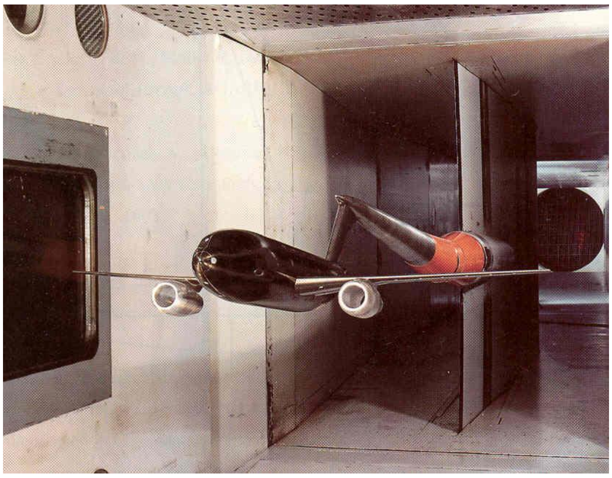

Figure 3.4 – Wind tunnel model

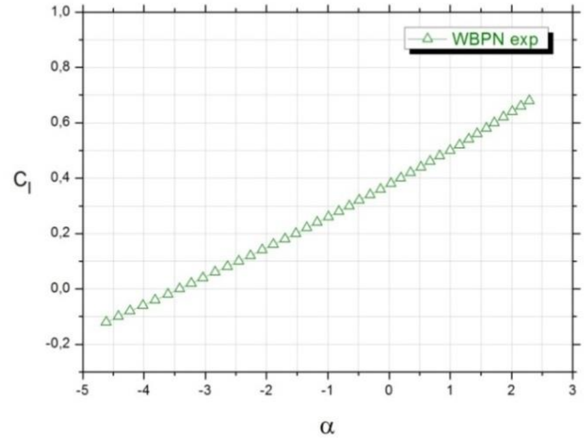

Figure 3.5 – Cl vs. angle of attack

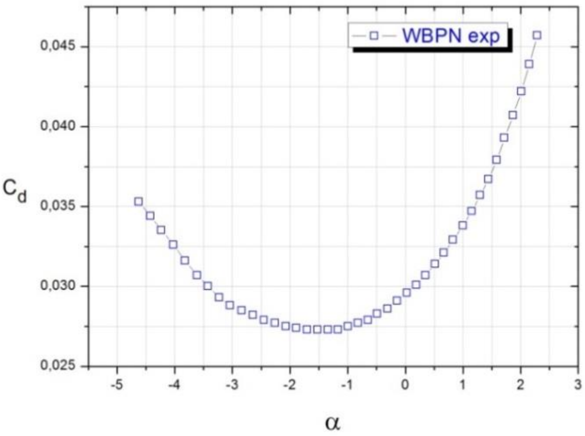

Figure 3.6 – Cd vs. angle of attack

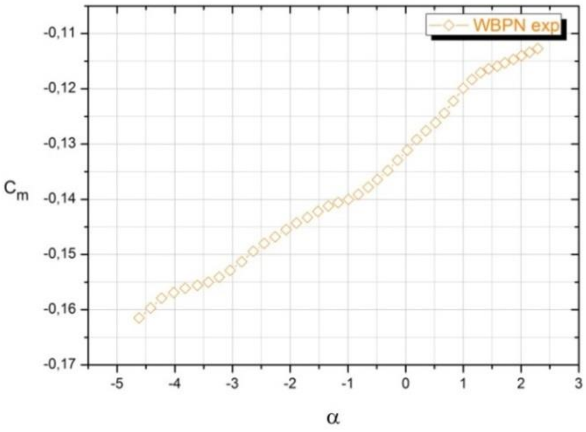

Figure 3.7 – Cm vs. angle of attack

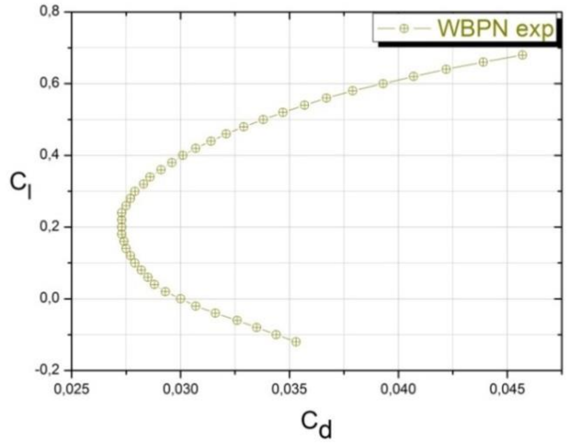

Figure 3.8 – Polar drag

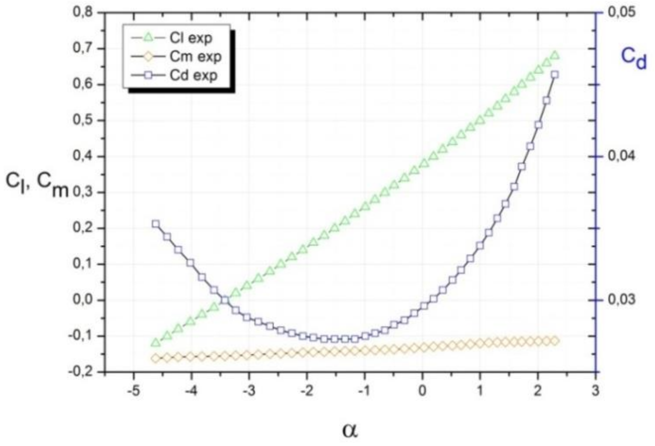

Figure 3.9 – Multiplot of Cl,Cd,Cm

Pressure coefficient related to wind tunnel experiment will be show in chapter 6, from Figure 6.11 to Figure 6.18.

Parameters which have been changed for morphing are commented in following sections.

3.2.1 Nacelle and pylon

The nacelle is a cover housing (separated from the fuselage) that holds engines, fuel, or equipment on an aircraft and it is usually positioned under the wing. The arrangement of engines influences the aircraft in many important ways. Safety, structural weight, flutter, drag, control, maximum lift, propulsive efficiency, maintainability, and aircraft growth potential are all affected. Engines may be placed in the wings, on the wings, above the wings, or suspended on pylons below the wings. They may be mounted on the aft fuselage, on top of the fuselage, or on the sides of the fuselage. Wherever the nacelles are placed, the detailed spacing with respect to wing, tail, fuselage, or other nacelles is crucial. When only the aerodynamic efficiency is considered, the nacelle position tends to be away from the wing.

DLR-F6 has a wing-mounted nacelles as the most of passengers aircraft. A typical engine for DLR-F6, CFM-56, is shown in Figure 3.10.

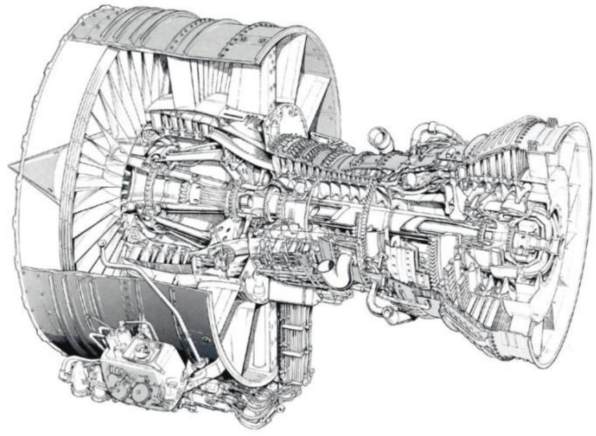

Figure 3.10 – CFM-56 engine and related features

Property	Value
S/2	72700 mm^2
c	141.2 mm
b/2	585.647 mm
AR	9.5
X_{ref}	157.9 mm
Y_{ref}	0mm
Z_{ref}	-33.92 mm
M_{cruise}	0.75
$C_{Lcruise}$	0.5
Re_{cruise}	3 x 10^6

Nacelle position is defined by three design variables: translation along z axis and x axis and rotation around y axis.

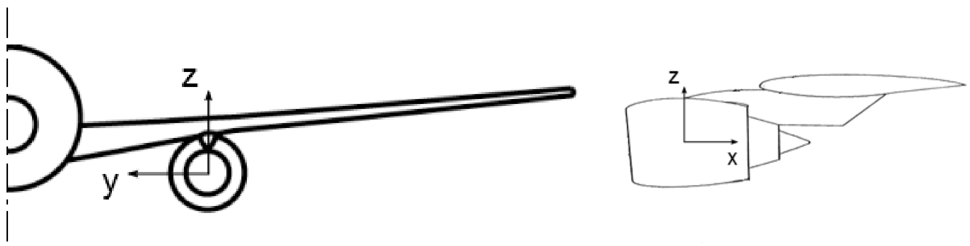

Figure 3.11 - Nacelle local axes

Amplification values, which are implemented with RBF-Morph, must be multiplied by the displacement used in mesh parametrization. The displacement is 1 mm for translations and one degree for rotation.

- Translation along z axis [-1; 1];
- Translation along x axis [-1; 1];
- Rotation around y axis [-1; 1].

Real displacements are presented in millimetres and they are referred to the wind tunnel model which is a scaled model:

- Traslation along z axis [-1 mm; 1 mm];
- Traslation along x axis [-1 mm; 1 mm];
- Rotation around y axis [-1°; 1°].

3.2.2 Sweep angle

As an aircraft enters the transonic speed just below the speed of sound, an effect known as *wave drag* starts to appear. Using conservation of momentum principles in the direction normal to surface curvature, airflow accelerates around curved surfaces, and near the speed of sound the acceleration can cause the airflow to reach supersonic speeds. When this occurs, an oblique shock wave is generated at the point where the flow slows down back to subsonic speed. Since this occurs on curved areas, they are normally associated with the upper surfaces of the wing.

Shock waves require energy to form. This energy is taken out of the aircraft, which has to supply extra thrust to make up for this energy loss. Thus the shocks are seen as a form of drag. The shocks form when the local air velocity reaches supersonic speeds over various features of the aircraft, this air velocity belongs to "critical Mach" speed where this effect becomes noticeable.

Aircrafts in the subsonic range just below the speed of sound need swept wings for increasing *Critical Mach number* in order to decrease drag and delay the drag rise caused by fluid compressibility.

The effect of sweepback on the critical Mach number of finite wings is usually analyzed in terms of a wing of given aspect ratio and airfoil thickness ratio in the free-stream direction. The airfoil thickness ratio normal to the leading edge varies, in this case, as the wing sweepback angle is changed. The swept wing must be regarded as a cornerstone of the aerodynamic design of modern high-subsonic-speed jet airplanes. As compared with a straight wing, the swept wing offers significant increases in cruising Mach number and, at the same time, permits the use of wings of sufficient thickness to allow aspect ratios high enough for good values of the maximum lift-to-drag ratio.

The aspect ratio, sweep angle, airfoil thickness ratio, and wing weight necessary for adequate wing strength and stiffness are all related and require a complex series of trade-off studies to arrive at an optimum design for a given set of requirements. The internal volume required for fuel storage and landing-gear retraction also forms an important part of these trade-off studies.

Swept wings effects on the aerodynamic physics are:

- Delayed Drag Rise
- Aerodynamic Center Moved Aft
- Heavier Structure
- Pitch up at stall
- Aeroelastic concerns

The angle of sweep which characterizes a swept wing is conventionally measured along the 25% chord line. If the 25% chord line varies in sweep angle, the leading edge is used.
DLR-f6 has 27,1° sweep angle as shown in Figure 3.12. Most common swept wings have angles from 25° to 30°.

In the present research two sweep angles will be considered, shape modifications consists in the variation of the sweep of the wing inner section **(a)** and of the outer section **(b)** as depicted in Figure 3.12.

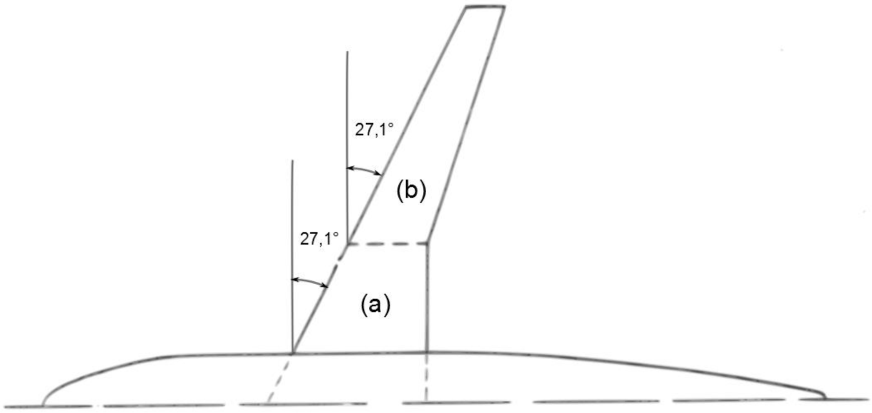

Figure 3.12 - Sweep angles definition

A reasonable range for both sweep angles is ±1°.

3.2.3 Dihedral angle

The angle that the wing makes with the local horizontal is called *dihedral angle*. Dihedral is added to the wings for roll stability; a wing with some dihedral will naturally return to its original position if it encounters a slight roll displacement. Most large airliner wings are designed with diherdral. The wing tips are farther off the ground than the wing root. Highly maneuverable fighter planes, on the other hand do not have dihedral. In fact, some fighter aircraft have the wing tips lower than the roots giving the aircraft a high roll rate. A negative dihedral angle is called anhedral.

Dihedral angle influences dihedral effect and stability, moreover nacelle size should be considered in order to be sure to have enough space between the ground and the wing.

DLR-f6 has a dihedral angle of 4,8° as depicted in Figure 3.13.
This shape modification will be from 3,8° to 5,8°.

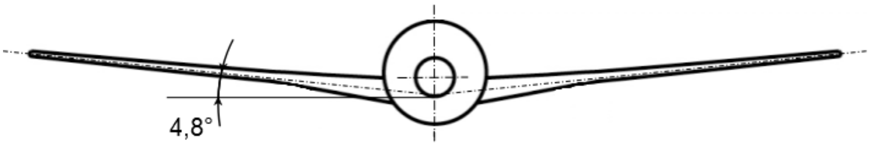

Figure 3.13 - Dihedral angle definition

3.2.4 Twist angle

Wing twist is a useful aerodynamic feature which is added to aircraft wings to adjust lift distribution along the wing, to maintain desired pressure and to decrease induced drag.

Often, the purpose of lift redistribution is to ensure that the wing tip is the last part of the wing surface to stall, for example when executing a roll or steep climb; it involves twisting the wingtip a small amount downwards in relation to the rest of the wing. This ensures that the effective angle of attack is always lower at the wingtip than at the root, meaning the root will stall before the tip. This is desirable because the aircraft flight control surfaces are often located at the wingtip, and the variable stall characteristics of a twisted wing alert the pilot to the advancing stall while still allowing the control surfaces to remain effective, meaning the pilot can usually prevent the aircraft from stalling fully before control is completely lost.

Twist that decreases the local chord incidence from root to tip is sometimes referred to as *washout*. Twist that increases the local incidence from root to tip is less common and is called *wash-in*.

Twist can be achieved in two ways. The most commonly used method is called *geometric twist*. When pure geometric twist is employed, the wing cross section at each location along the wingspan has an airfoil shape that is geometrically similar to that of the root cross section. Another method sometimes used to effectively twist a wing is called *aerodynamic twist*. For a wing with pure aerodynamic twist, the chord line of the airfoil cross section at each location along the span of the wing is exactly parallel with the chord line of the root airfoil section.

DLR-f6 model has geometric and aerodynamic twist already and changing this feature can seriously compromise stability.

In the present work twist angle consists in a rigid rotation of two sections (both sections are parallel to the symmetry plane) at the kink and at the tip of the wing around two axes. Both axes are orthogonal to the symmetry plane of the aircraft and intersect the wing at the leading edge, the first one at the kink (a) and the second one at the tip (b).

Both twist angle ranges will be ±1° from the default configuration.

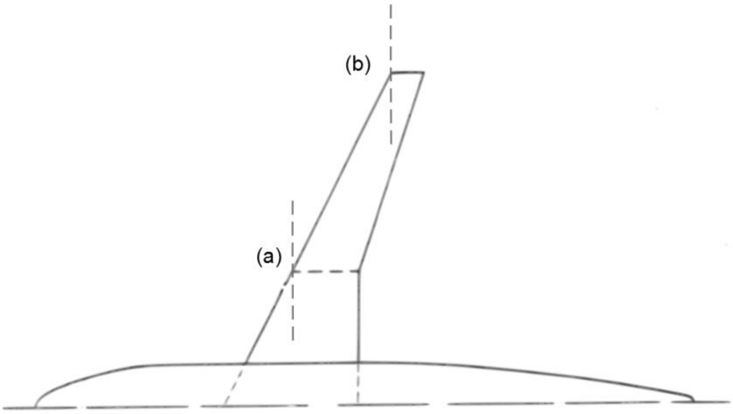

Figure 3.14 - Axes definition for twisting: (a) kink, (b) tip

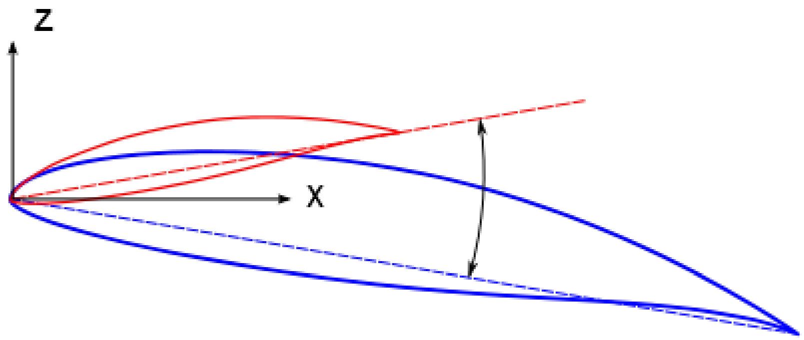

Figure 3.15 - Wing twist; two wing sections: tip (red), root (blue)

4 RADIAL BASIS FUNCTIONS

4.1 RBF theory

A system of RBFs is used to produce a solution for the mesh movement/morphing, from a list of source points and their displacements.

RBFs are powerful mathematical functions able to interpolate, giving the exact values in the original points, functions defined at discrete points only (source points) in a n-dimensional environment. The behaviour of the function between points and the interpolation quality depends on the kind of basis adopted. Using RBFs can be indeed modified the displacement at discrete points, and interpolated congruently every nodal position of the grid in a mesh independent fashion, as it deals with points positions only.

Typical RBF with global and compact support are shown in Table 4.1. It should be noted that RBF is a scalar function with the scalar variable r, which is the Euclidean norm of the distance between two points r defined in a generic n-dimensional space (with n equal to 2 and 3 for 2D and 3D appications respectively).

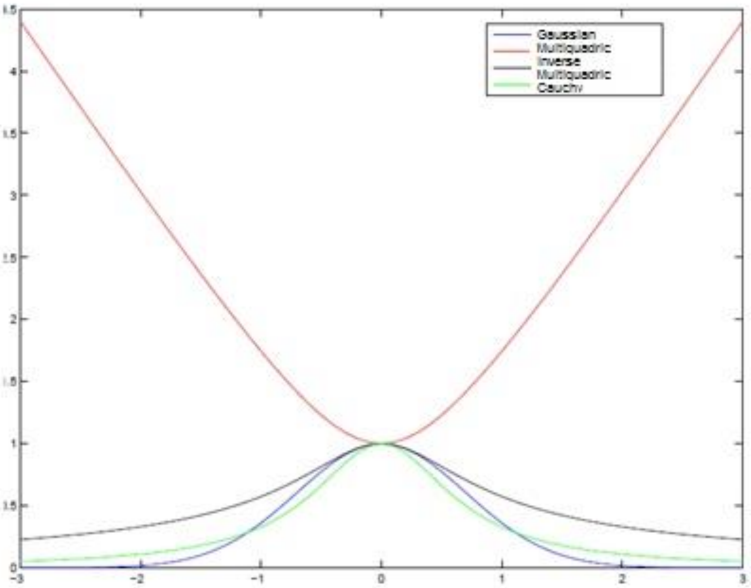

Figure 4.1 – RBFs: gaussian, multiquadric, inverse multiquadric, cauchy

Table 4.1 – Typical RBFs

Radial Basis Functions(RBF) with global support	$\varphi(r), r = \|r\|$
Spline type (R_n)	$r^n, nodd$
Thin plate spline (TPS_n)	$r^n log(r), neven$
Multiquadric (MQ)	$\sqrt{1+r^2}$
Innverse multiquadric (IMQ)	$\frac{1}{\sqrt{1+r^2}}$
Inverse quadratic (IQ)	$\frac{1}{1+r^2}$
Gaussian (GS)	e^{-r^2}
Radial Basis Functions(RBF) with compact support	$\varphi(r) = f(\xi), \xi \leq 1, \xi = \frac{r}{R_{sup}}$
Wendland C^0 (C0)	$(1-\xi)^2$
Wendland C^2 (C2)	$(1-\xi)^4(4\xi+1)$
Wendland C^4 (C4)	$(1-\xi)^6\left(\frac{35}{3}\cdot\xi^2+6\xi+1\right)$

As it will be shown in detail, a linear system of equations (of order equal to the number of source point introduced) needs to be solved for the coefficients calculation. Once the unknown coefficients are calculated, the motion of an arbitrary point inside or outside the domain (interpolation/extrapolation) is expressed as the sum of the radial contribution of each source point (if the point falls inside the influence domain).

Details of this theory need to be given using some equations. An interpolation function composed of a radial basis and a polynomial is defined as follows:

$$\boldsymbol{s(x) = \sum_{i=1}^{N} \Upsilon_i \varphi(||x - x_{ki}||) + h(x)} \qquad 4.1$$

The degree of the polynomial has to be chosen depending on the kind of RBF adopted. A radial basis fit exists if the coefficients γ_i and the weights of the polynomial can be found such that the desired function values are obtained at source points and the polynomial terms gives no contributions at source points, that is:

$$\boldsymbol{s(x_{ki}) = g_{i,} \quad 1 \le i \le N} \qquad 4.2$$

$$\boldsymbol{\sum_{i=1}^{N} \Upsilon_i q(x_{ki}) = 0} \qquad 4.3$$

for all polynomials *q* with a degree less or equal to that of polynomial *h*. The minimal degree of polynomial *h* depends on the choice of the RBF. A unique interpolant exists if the basis function is a conditionally positive definite function. If the RBFs are conditionally positive definite of order m ≤ 2, a linear polynomial can be used:

$$\boldsymbol{h}(\boldsymbol{x}) = \boldsymbol{\beta}_1 + \boldsymbol{\beta}_2\boldsymbol{x} + \boldsymbol{\beta}_3\boldsymbol{y} + \boldsymbol{\beta}_4\boldsymbol{z} \tag{4.4}$$

The subsequent exposition will assume that the aforementioned hypothesis is valid. A consequence of using a linear polynomial is that rigid body translations are exactly recovered. The values for the coefficients γ_i of RBF and the coefficients β of the linear polynomial can be obtained by solving the system:

$$\begin{pmatrix} \boldsymbol{M} & \boldsymbol{P} \\ \boldsymbol{P^T} & \boldsymbol{0} \end{pmatrix} \begin{pmatrix} \boldsymbol{\gamma} \\ \boldsymbol{\beta} \end{pmatrix} = \begin{pmatrix} \boldsymbol{g} \\ \boldsymbol{0} \end{pmatrix} \tag{4.5}$$

where g are the know values at the source points. M is the interpolation matrix defined calculating all the radial interactions between source points:

$$\boldsymbol{M_{ij}} = \boldsymbol{\varphi}\left(\left\|\boldsymbol{x_{k_i}} - \boldsymbol{x_{k_j}}\right\|\right), \quad \boldsymbol{1 \le i \le N}, \;\; \boldsymbol{1 \le j \le N} \tag{4.6}$$

and P is a constraint matrix that arises to balance the polynomial contribution and it contains a column of "1" and the $x\,y\,z$ positions of source points in the others three columns:

$$\mathbf{P} = \begin{pmatrix} 1 & x_{k_1} & y_{k_1} & z_{k_1} \\ 1 & x_{k_2} & y_{k_2} & z_{k_2} \\ \vdots & \vdots & \vdots & \vdots \\ 1 & x_{k_N} & y_{k_N} & z_{k_N} \end{pmatrix} \tag{4.7}$$

Radial basis interpolation works for scalar fields. For the smoothing problem each component of the displacement field prescribed at the source points is interpolated as follows:

$$\begin{cases} s_x(x) = \sum_{i=1}^{N} \Upsilon_i^x \varphi(\|x - x_{ki}\|) + \beta_1^x + \beta_2^x x + \beta_3^x y + \beta_4^x z \\ s_y(x) = \sum_{i=1}^{N} \Upsilon_i^y \varphi(\|x - x_{ki}\|) + \beta_1^y + \beta_2^y x + \beta_3^y y + \beta_4^y z \\ s_z(x) = \sum_{i=1}^{N} \Upsilon_i^z \varphi(\|x - x_{ki}\|) + \beta_1^z + \beta_2^z x + \beta_3^z y + \beta_4^z z \end{cases} \quad 4.8$$

Radial basis method has several advantages that make it very attractive for mesh smoothing. The key point is that being a meshless method only grid points are moved regardless of which elements are connected and it is suitable for parallel implementation. In fact, once the solution is known and shared in the memory of each calculation node of the cluster, each partition has the ability to smooth its nodes without taking care of what happens outside because the smoother is a global point function and the continuity at interfaces is implicitly guaranteed.

4.2 RBF-Morph

In order to explore a wide range of aircraft configurations RBF-Morph has been used.

The use of RBF-Morph allows the CFD user to perform shape modifications, compatible with the mesh topology, directly in the solving stage, just adding one single command line in the input file. In this way it is possible to perform fast mesh morphing using a mesh-independent approach based on state-of-the-art RBF (*Radial Basis Functions*) techniques without the need of producing a new cad model and a new mesh for each configuration.

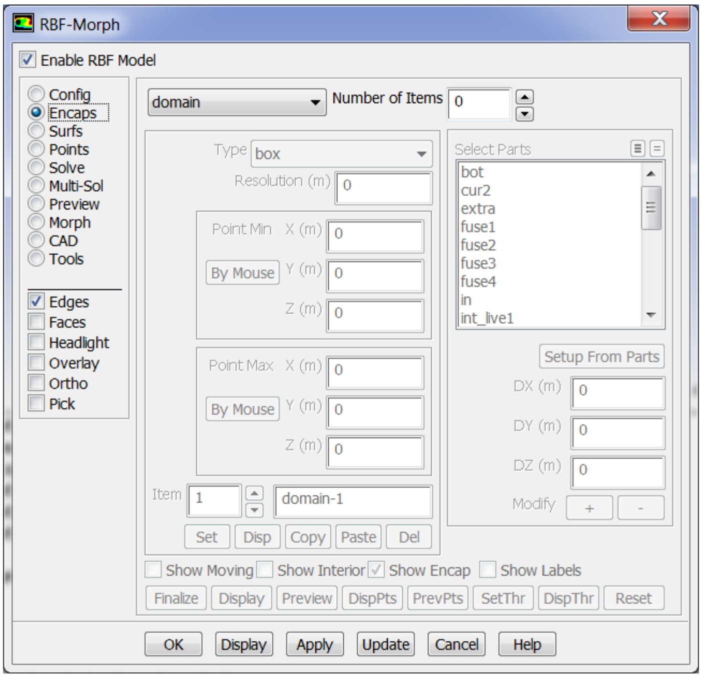

☑ Enable RBF Model
● Encaps
☑ Edges
☐ Faces
☐ Headlight
☐ Overlay
☐ Ortho
☐ Pick
domain
Number of Items 0
Type box
Resolution (m) 0
Point Min X (m) 0
Y (m) 0
Z (m) 0
Point Max X (m) 0
Y (m) 0
Z (m) 0
DX (m) 0
DY (m) 0
DZ (m) 0
Item 1 domain-1
☐ Show Moving ☐ Show Interior ☑ Show Encap ☐ Show Labels

Figure 4.2 – RBF-Morph grafic interface

The most important specifications are:

- full integration with *ANSYS Workbech* and *ANSYS Fluent* with a dedicated GUI (graphic interface) and TUI (text interface),
- modification of the original surface and volume mesh producing a nodal smoothing without changing the mesh topology,
- mesh-independent solution,
- parallel morphing of the grid,
- large size models (many million of cells) can be morphed in a reasonable short time,
- management of every kind of mesh element type (tetrahedral, hexahedral, polyhedral, prismatic, hexcore, non-conformal interfaces, etc.),
- multiple value settings allows parametric morphing,
- support of the CAD re-design of the morphed surfaces.

A complete mesh morphing by means of RBF-Morph can be divided in three steps:

- source points definition,
- RBF System solution,
- mesh morphing for the surface and/or volume.

The first step consists in implementing graphical user interface in a serial fashion, interacing directly with the needed tool. To easily define the problem source points can be selected using surfaces, picking directly the interested points or restricting the morpher action using an encap panel.

After problem definition the RBF solution can be calculated. The resulting configuration can be previewed and overimposed over the original mesh without actually modifying the original grid. Final quality can be checked and source points saved if needed. Solutions for each desired modifier can be saved as well.

The last step can be performed in serial or in parallel with or without the GUI. Once the solutions are available, they can be loaded and used to morph the mesh using the Morph panel of the GUI or using TUI commands that allow to prescribe a single morph or a multi-morph, combining the effect of multiple modifiers. Considering that each modifier can be applied with the desired magnitude (Amplification), a parametric Fluent model results and DOE analysis can be carried taking advantage of the included dedicated options.

4.2.1 Morphing optimization

LCM Distance is the *Local Correction Method* (LCM) distance used to reduce the total number of source points. It operates in a similar way with respect to the sub-sampling technique but without losing the accuracy of the surfaces at least within the solver tolerance. With the LCM approach a problem of several hundreds of thousands of points can be solved in a reasonable time. Usually, this parameter should be set reaching a trade-off between the dimension of the reduced problem and the LCM operation costs. Some trial-and-error are sometime necessary to work out the best value for the LCM Distance. If this parameter is set to zero, no LCM will be used.

An LCM optimization has been carried before morphing in this thesis. The LCM value that permits a faster morphing solution has proven to be 0.01 as shown in graph.

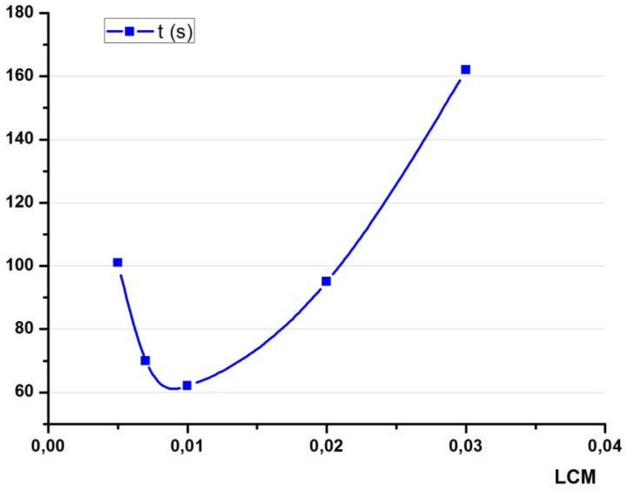

Figure 4.3 – Calculation time of number of source points vs. LCM

Other useful optimization have been done following a simple "*rule of thumb*" for *Domain Encap* and its *Resolution*.

<u>Domain Encap</u> defines the boundary of the morphing domain and if activated everything outside (surface and volume mesh) is not affected by the RBF solution. It is suitably designed to restrict the morphing action within a part of the model only.

<u>Resolution</u> controls the number of points that are created equally spaced on the Encap surface. The resolution is defined as the approximate distance between the points on the surface. The chosen combination of these two features is a *Domain* of 1026 points with a *Resolution* of 0.04 m.

5 SIMULATIONS

5.1 Mesh definition

The partial differential equations that govern fluid flow and heat transfer are not usually amenable to analytical solutions, except for very simple cases. Therefore, in order to analyze fluid flows, flow domains are split into smaller subdomains (made up of geometric primitives like hexahedra and tetrahedra in 3D and quadrilaterals and triangles in 2D). The governing equations are then discretized and solved inside each of these subdomains. Care must be taken to ensure proper continuity of solution across the common interfaces between two subdomains, so that the approximate solutions inside various portions can be put together to give a complete picture of fluid flow in the entire domain. The subdomains are often called elements or cells, and the collection of all elements or cells is called a mesh or grid. The origin of the term mesh (or grid) goes back to early days of CFD when most analyses were 2D in nature. For 2D analyses, a domain split into elements resembles a wire mesh, hence the name.

The process of obtaining an appropriate mesh (or grid) is termed mesh generation (or grid generation), and has long been considered a bottleneck in the analysis process due to the lack of a fully automatic mesh generation procedure. Specialized software programs have been developed for the purpose of mesh and grid generation, and access to a good software package and expertise in using it are vital to the success of a modeling effort.

The most basic form of mesh classification is based upon the connectivity of the mesh: structured or unstructured.

A *structured mesh* is characterized by regular connectivity that can be expressed as a two or three dimensional array. This restricts the element choices to quadrilaterals in 2D or hexahedra in 3D. The regularity of the connectivity allows us to conserve space since neighborhood relationships are defined by the storage arrangement. Additional classification can be made upon whether the mesh is conformal or not.

An *unstructured mesh* is characterized by irregular connectivity and it is not readily expressed as a two or three dimensional array in computer memory. This allows for any possible element that a solver might be able to use. Compared to structured meshes, the storage requirements for an unstructured mesh can be substantially larger since the neighborhood connectivity must be explicitly stored.

A *hybrid mesh* is a mesh that contains structured portions and unstructured portions. There is disagreement as to the correct application of the terms "hybrid" and "mixed." The term "mixed" is usually applied to meshes that contain elements associated with structured meshes and elements associated with unstructured meshes (presumably stored in an unstructured fashion).

Mesh quality can be evaluated by means of some parameters.

- *Clustering*
  Mesh clustering is to partition the faces or vertices of the mesh into different regions. Generally, these regions are required to be nonoverlapping and connected.

- *Skewness*
  The skewness of a grid is the most important indicator of the mesh quality and suitability. Large skewness compromises the accuracy of the interpolated regions. It indicates how much a face is similar to the equiangular one. A Skewness of 0 is the best possible one and a skewness of one is almost never preferred. For hex and quad cells, skewness should not exceed 0.85 to obtain a fairly accurate solution. For Triangular cells,

skewness should not exceed 0.85 and for Tetragonal cells, skewness should not exceed 0.9.

There are three methods of determining the skewness of a grid.

- Based on equilateral volume

This method is applicable to triangles and tetrahedral only and is the default method.

$$\text{Skewness} = \frac{\text{optimal celle size} - \text{cell size}}{\text{optimal celle size}}$$

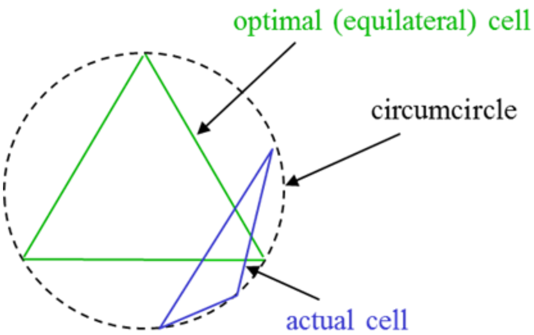

Figure 5.1 – Mesh skewness

- Based on the deviation from normalized equilateral triangle

This method applies to all cell and face shapes and is almost always used for prisms and pyramids

$$\text{Skewness} = \max\left[\frac{\theta_{max} - 90}{90}, \frac{90 - \theta_{min}}{90}\right]$$

- Equiangular skew

Another common measure of quality is based on equiangular skew.

$$\text{Skewness} = \max[\frac{\theta_{max} - \theta_e}{180 - \theta_e}, \frac{\theta_e - \theta_{min}}{\theta_e}]$$

Where:

θ_{max} = largest angle in a face or cell

θ_{min} = the smallest angle in a face or cell

θ_e = the angle for equi-angular face or cell (60 for a triangle, 90 for a square)

- *Aspect ratio*

  It is the ratio of longest to the shortest side in a cell. Ideally it should be equal to 1 to ensure best results. For multidimensional flow, it should be near to one. Also local variations in cell size should be minimal, i.e. adjacent cell sizes should not vary by more than 20%. Having a large aspect ratio can result in an interpolation error of unacceptable magnitude.

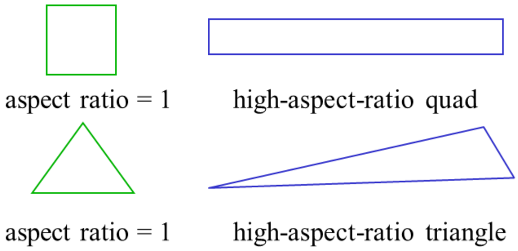

Figure 5.2 – Mesh aspect ratio

- *Smoothness*

  The change in size should be smooth. There should not be sudden jumps in the size of the cell because this may cause erroneous results at nearby nodes.

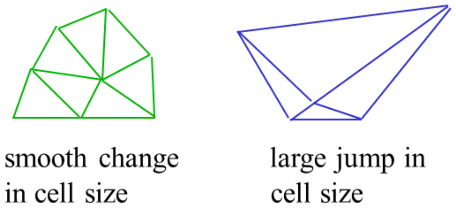

Figure 5.3 – Mesh smoothness

In the present workflow two kind of meshes have been studied in order to prove the meshless property of RBF-Morph; both meshes, a coarse one with 3 million of cells and a fine one with 14 million of cells, are *hybrid* and *unstuctured* as shown in Figure 5.4 and Figure 5.5 related to the coarse and fine mesh rispectively.

Meshes were taken from the Nasa web site (2° DPW), carried out with *ICEM*, a professional meshing software, and finally studied with *ANSYS Fluent*.

Related values about meshes such as cells, faces, nodes and quality are reported in Table 5.1.

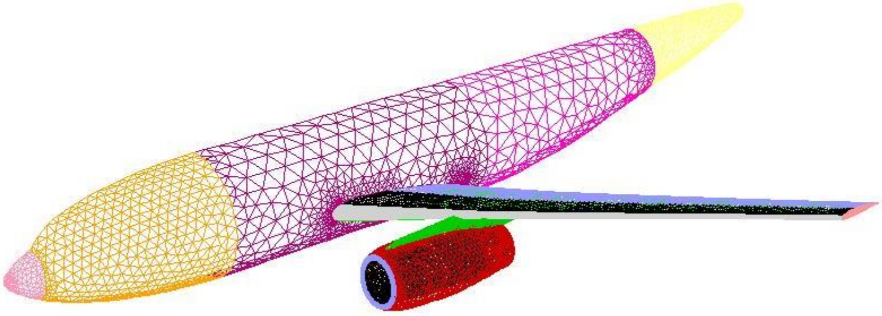

Figure 5.4 – Surface mesh of the 3 million of cells mesh model

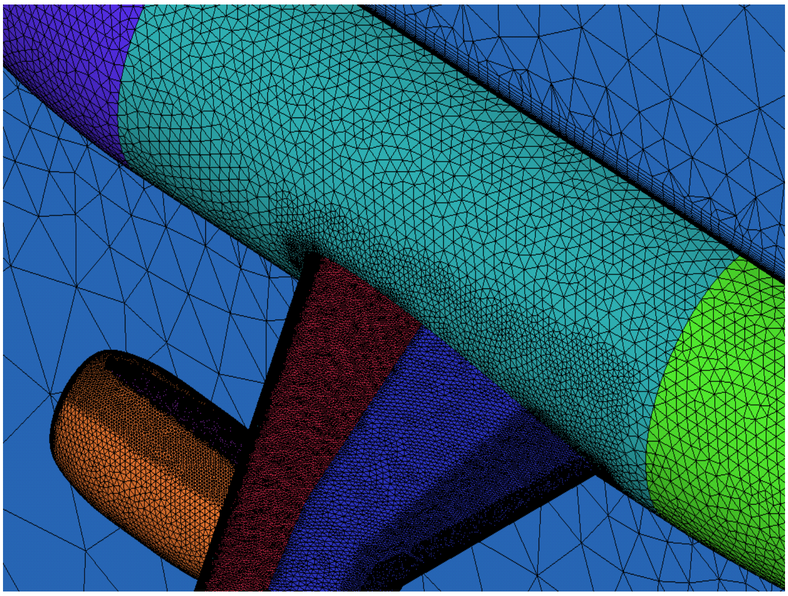

Figure 5.5 – Surface mesh of the 14 million of cells mesh model

Table 5.1 – Mesh dimensions and quality

MESH	Cells	Faces	Nodes
Coarse	2929321	6776292	1089953
Fine	13641888	32724676	5887240

Mesh Quality			
Type	Minimum Orthogonal Quality	Maximum Aspect Ratio	Maximum Skewness
Coarse	9.02621e-02	9.77633e+02	0.8846979
Fine	4.20095e-3	1.25469e+04	0.985118

As shown in Table 5.1, mesh skewnees of the fine mesh excesses 0.95 in the nearness of the pylon, for this reason nacelle displacements are strictly limited. Mesh is divided in several parts in order to facilitate calculation, get fluid dynamic values related to part of the airplane and set boundary conditions.

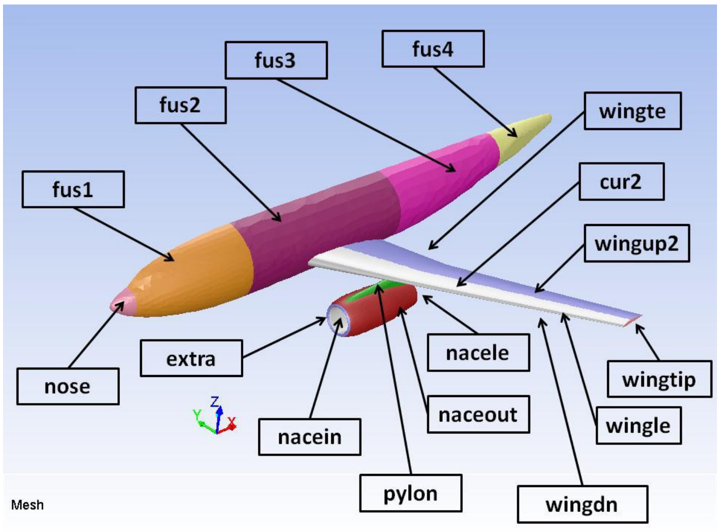

Figure 5.6 – Model surface definition

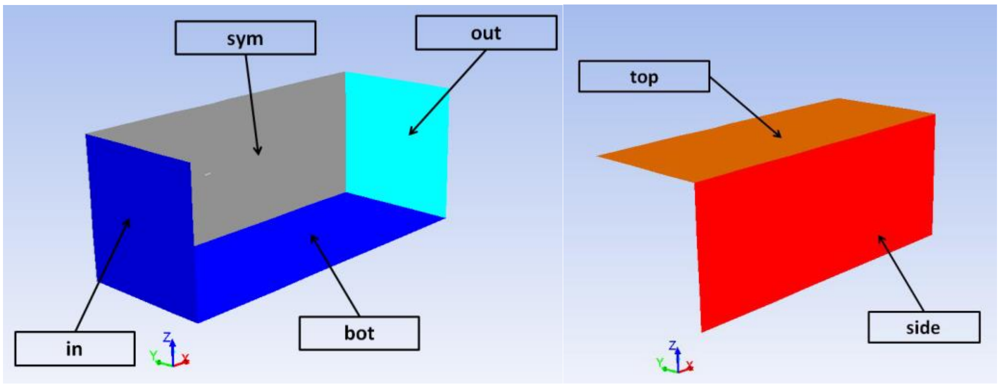

Figure 5.7 – Names of the wind tunnel boundary walls

5.2 Workflow

The whole workflow has been performed using *ANSYS Fluent* for fluid dynamic run and *ANSYS Workbench* for *DOE* automated run.

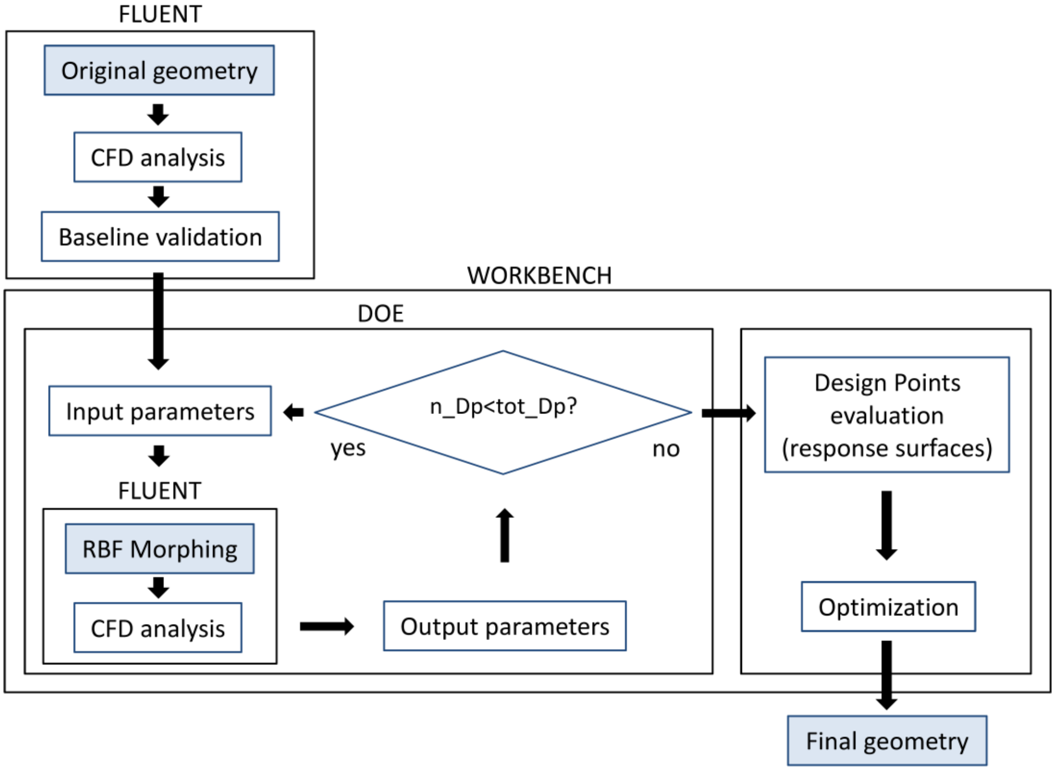

Figure 5.8 – Proposed workflow

The entire study has been carried using an HP Z820 Workstation with the following features:

- Processors: 2 Intel(R) Xeon(R) CPU E5-2680 0 @ 2.70 GHz Eight-core.
- Installed memory RAM: 128 Gb
- Operating sistem: Genuine Windows 7 Professional 64-bit

5.2.1 Baseline

The first step consisted in studying a baseline so as to have a starting point used for the next simulations during the DOE where 81 design points have been tested.

Baseline settings are explained in the next passages.

- *General*

  Density-based solver has been chosen because this solver is suitable for compressible fluids with high Reynolds numbers and a strong coupling or interdipendence between density energy and momentum. The flow has been considered steady.

- *Models*

  Turbulence model is *Spalart-Allmaras*, this model is decidely an aeronautic turbulence model.

- *Materials*

  The fluid considered is air as a ideal gas with a temperature of 305 K.

- *Boundary conditions*

  DLR-F6 has an attack angle of 1° in cruise conditions so *in* (inlet), *bot*, *top* and *side* surfaces have been set as *pressure-*

far-field with a Mach number of 0,75 corresponding to a speed of about 260 m/s with related angles for velocity components.

Symmetry has been applied for the symmetry plane and the whole aircraft surfaces has been set as *wall* with the aluminium default values with *no-slip* conditions.

- *Reference values*

  Reference values has been calculated from inlet section (*in*) as shown in Figure 5.9

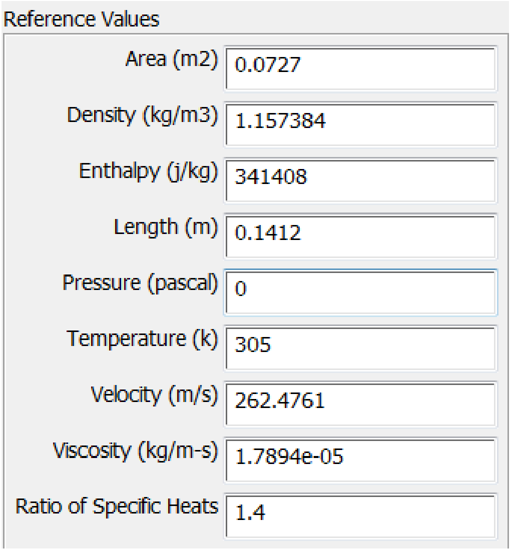

Reference Values

Area (m2): 0.0727
Density (kg/m3): 1.157384
Enthalpy (j/kg): 341408
Length (m): 0.1412
Pressure (pascal): 0
Temperature (k): 305
Velocity (m/s): 262.4761
Viscosity (kg/m-s): 1.7894e-05
Ratio of Specific Heats: 1.4

Figure 5.9 –Inlet reference values

- *Solution methods*

  Roe flux-difference splitting (Roe-FDS) with *explicit* formulation has been chosen with *Green-Gauss Node Based* as interpolation method because this method is the most accurate and avoid false diffusions. A second order accuracy has been set for the 3 million case.

- *Solution controls*

  First tests have been executed with default values of *Courant number* and *Under-Relaxation* factors for coarse mesh, then the former has been reduced to 0,75 to facilitate convergence. For fine mesh *Courant number* and *Under-Relaxation* factors where changed during calculation after 9000 step of iterations in order to accelerate convergence.

- *Solution inizialization*

  Standard initialization has been used for the coarse mesh, *FMG initialization (full multigrid initialization)* has been set for the finest mesh for a better initialization of the flow field.

5.2.1.1 Baseline results

As written in the previous section, the first run (baseline) has been executed in order to have a starting point for the DOE study and save a lot of computational time.

Baseline run went on 2500 iterations using a restricted convergence criterion for coarse mesh and about 13000 iterations for fine mesh. Computational time was 5 and 65 hours for coarse and fine meshes rispectively. In the following pages baseline graph about residuals, C_l, C_d and C_m are reported. Residuals give evidence that convergence is gained as well as C_l, C_d and C_m coefficients related to both meshes which have fluctuations under the fourth decimal figure.

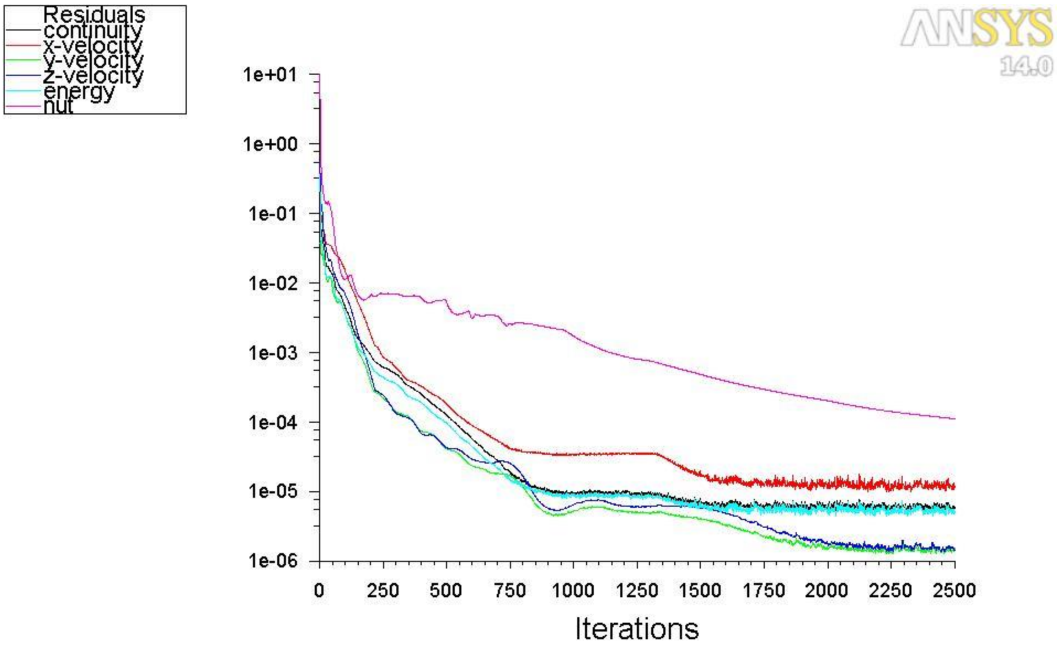

Figure 5.10 – Scaled residuals profiles, 3m of cells

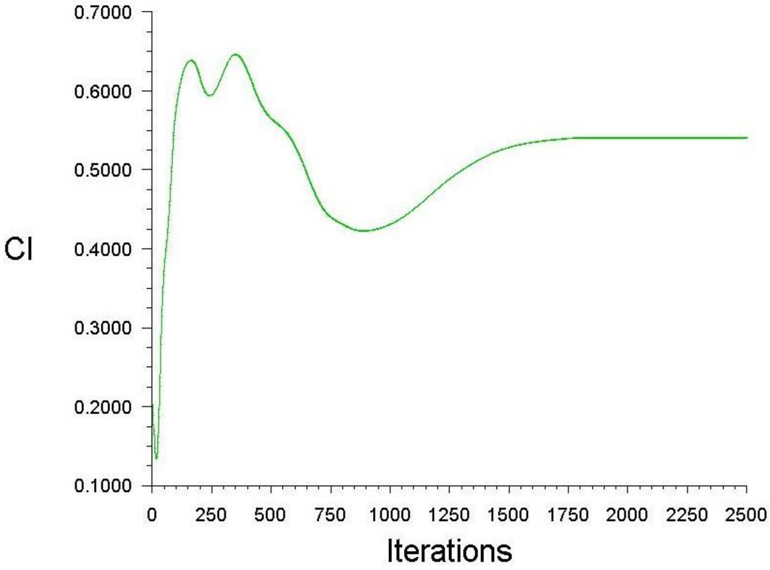

Figure 5.11 – Cl profile, 3m of cells

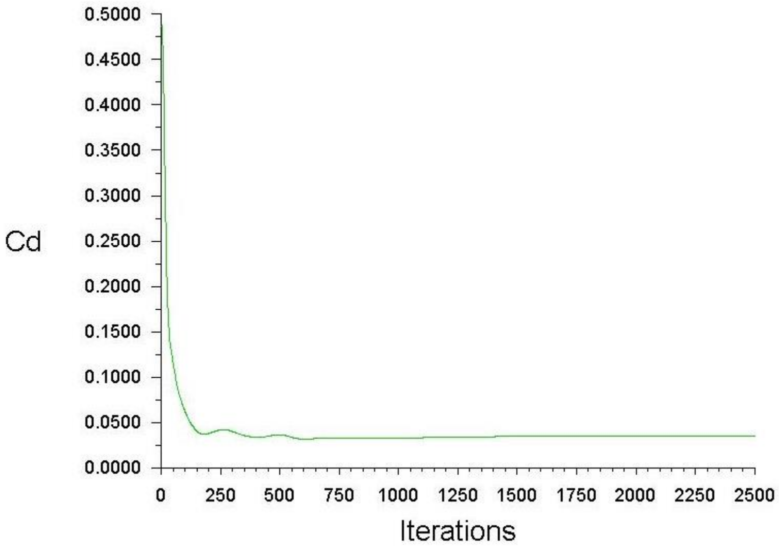

Figure 5.12 – Cd profile, 3 million of cells

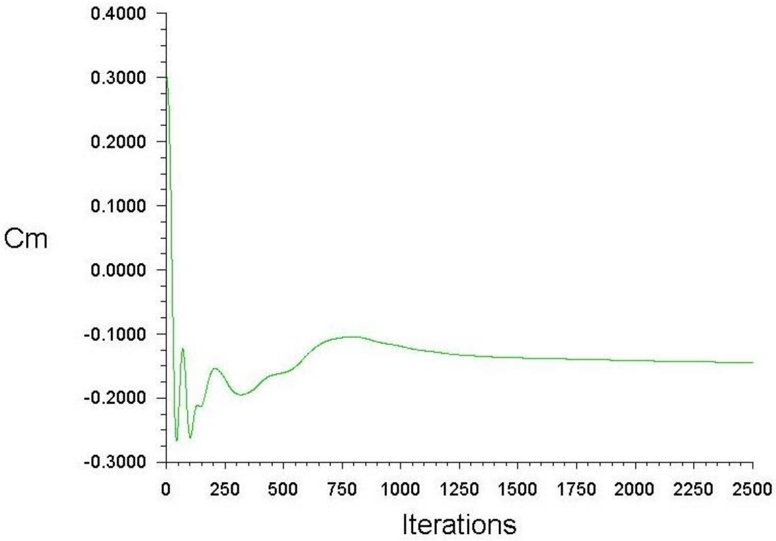

Figure 5.13 - Cm profile, 3 million of cells

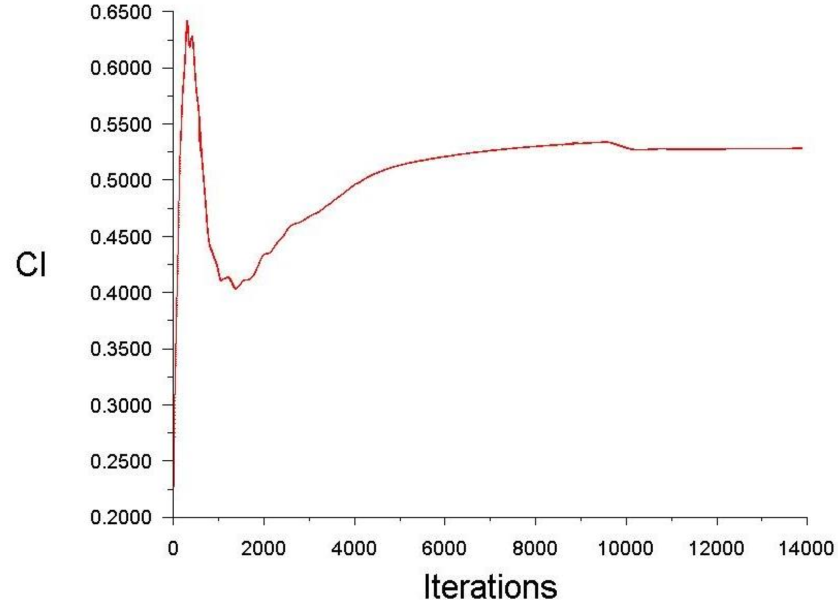

Figure 5.14 - Cl profile, 14 million of cells

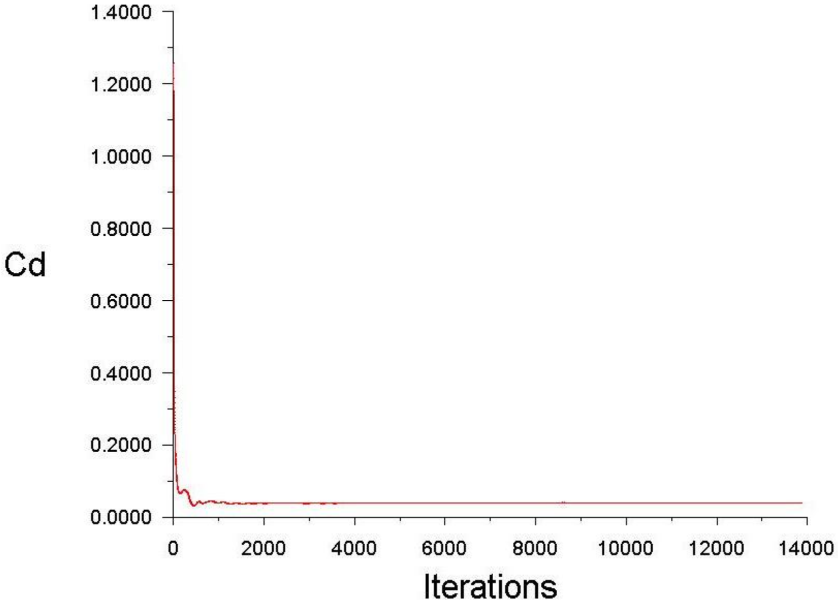

Figure 5.15 - Cd profile, 14 million of cells

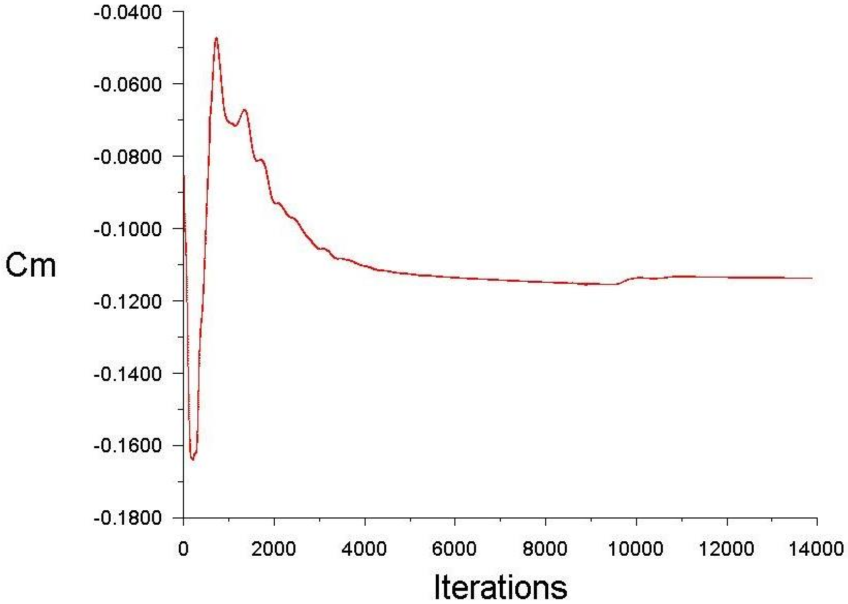

Figure 5.16 - Cm profile, 14 million of cells

Finally, the mass flow rate has been avaluated to prove that continuity equation is verified.

Mass flow rate is calculated with the formula: $\rho v_n = {}^{\dot{m}}/_{A}$

Where v_n is the velocity which is normal to the considered section, ρ is the density and it’s calculated with the ideal gas law $p = \rho RT$.

Table 5.2 - Mass flow rate, 3m and 14 m

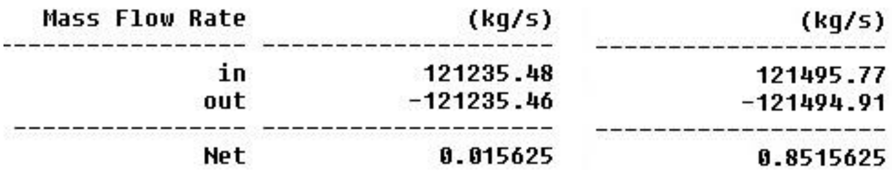

```
   Mass Flow Rate                 (kg/s)               (kg/s)
-----------------  --------------------   --------------------
               in             121235.48            121495.77
              out            -121235.46           -121494.91
 ----------------  --------------------   --------------------
              Net              0.015625            0.8515625
```

as depicted in table it can be infered that the net mass flow rate is less than 7*10e-4% for both meshes, this value is widely inferior than the reference value[3] (0,1%).

---

[3] Reference value, *Ansys FLUENT Theory guide,* pag. 256

5.2.2 Mesh morphing

The second step, not necessary subsequent to the first, was generating the morphing solutions for all parameters by means of RBF-Morph. As stated in previous chapter, eight parameters have been implemented, their amplification range are repeated here for a further information.

Nacelle displacements: traslation along z axis [-1 mm; 1 mm] and along x axis [-1 mm; 1 mm], rotation around y axis [-1°; 1°].
DLR-f6 has 27,1° sweep angle and most common aircraft have swept wing angles from 25° to 30°. A reasonable range for both sweep angles is ±1°.
DLR-f6 has a dihedral angle of 4,8°. This shape modification will be varied from 3,8° to 5,8°.
Both twist angle ranges of the considered airplane will be ±1° from default configuration.

It is important to remark that changing the above-mentioned features can seriously influence aircraft performance, safety and stability, therefore their ranges are rather restricted.

5.2.3 Design of experiments

The main step in this thesis workflow was the DOE. DOE is a fruitful technique used when a large number of experiments have to be accomplished. This method consists in defining a test plan with a restricted number of simulation in order to optimize computational time and simultaneously to obtain a wide and satisfactory range of design configurations.

DOE is essential for assuring the integrity and reproducibility of research findings, and design principles such as randomisation, replication and blocking have become standards of best practice in many areas.

A DOE has been implemented after calculating the baseline in order to find the best configuration for DLR-F6 combining eight above-mentioned parameters. A DOE table with 81 design points has been generated using

ANSYS Workbench with the *Optimal space filling (OSF)* method. *Optimal Space-Filling Design (OSF)* creates optimal space filling Design of Experiments plans according to some specified criteria. Essentially, *OSF* is a Latin Hypercube Sampling Design (*LHS*) that is extended with post-processing. It is initialized as an *LHS* and then optimized several times, remaining a valid *LHS* (without points sharing rows or columns) while achieving a more uniform space distribution of points (maximizing the distance between points)

OSF shares some of the same disadvantages as *LHS*, though to a lesser degree. Possible disadvantages of an *OSF* design are that extremes (i.e., the corners of the design space) are not necessarily covered and that the selection of too few design points can result in a lower quality of response prediction. In this manner a *DOE* table with equidistant points is gained. In the Figure 5.17 an example of design points distribution is shown with *Optimal Space Filling* sampling.

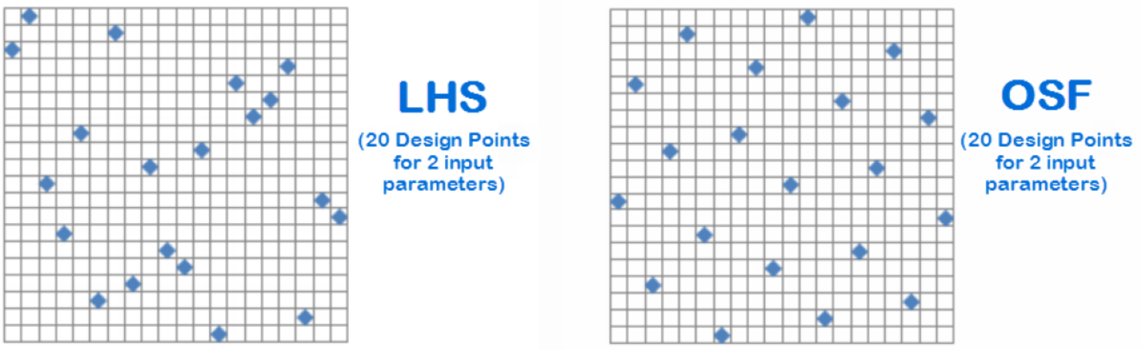

Figure 5.17 – LSH and OSF sampling

5.2.3.1 Design points

Using the above mentioned sampling method, a *DOE* table with 81 *Design Points* has been generated. In this section, design points and an analysis of the input and output parameters will be presented.

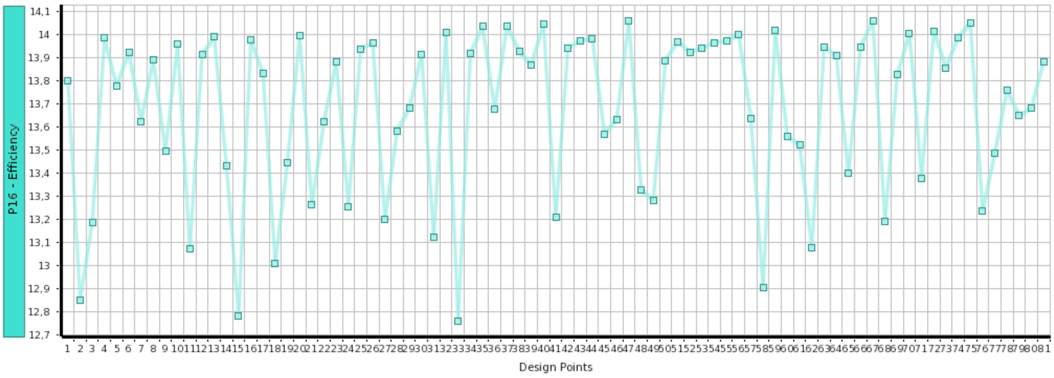

Figure 5.18 – Design points vs. efficiency

Predicted versus Observed Chart

In the chart view, a scatter chart presents for each output parameter the values predicted from the response surface versus the values observed from the design points. This chart lets you quickly determine if the response surface correctly fits the points of the *Design of Experiments* and the refinement table: the closer the points are to the diagonal line, the better the response surface fits the points. In this work a good fit of the response surface has been reached for both cases as depicted in following graphs.

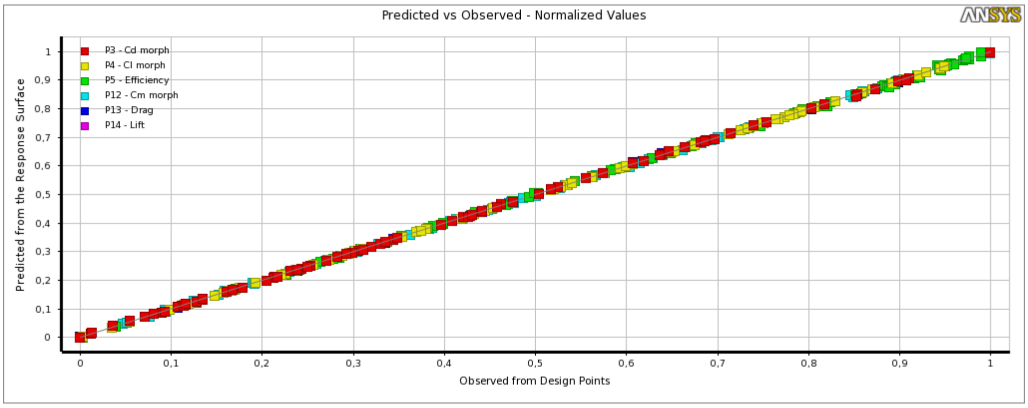

Figure 5.19 –Goodness of fit (coarse mesh)

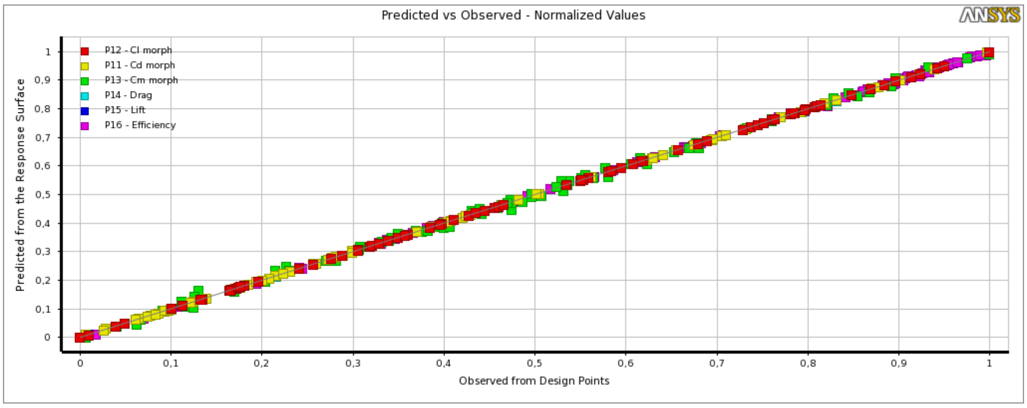

Figure 5.20 - Goodness of fit (fine mesh)

Local and global Sensitivity Charts

Local sensitivity chart allows you to graphically view the impact that changing each input parameter has on the output parameters.

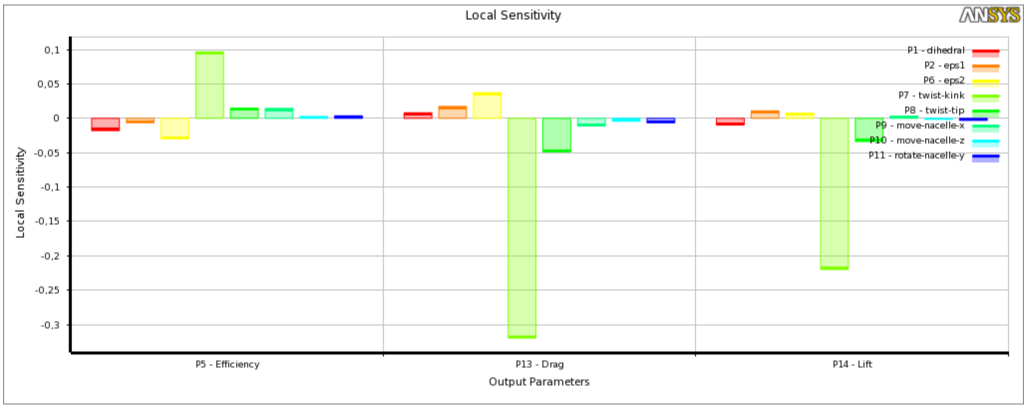

Figure 5.21 - Local Sensitivity Chart

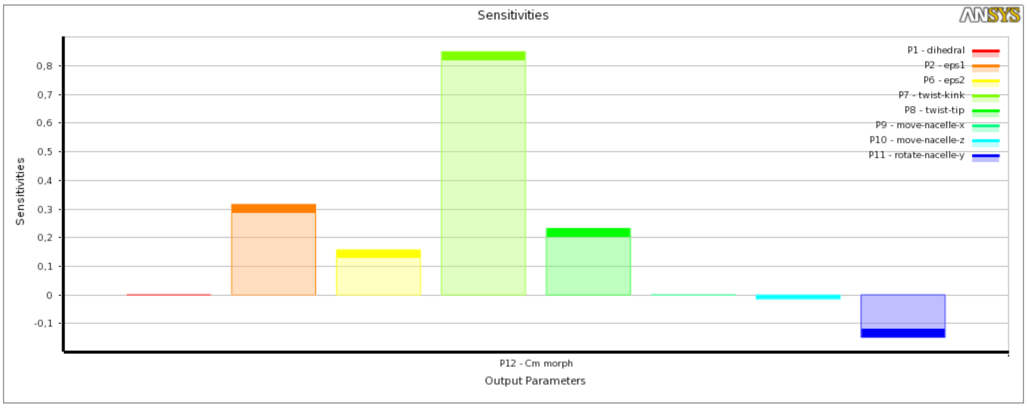

Figure 5.22 – Global sensitivity chart of Cm (coarse mesh)

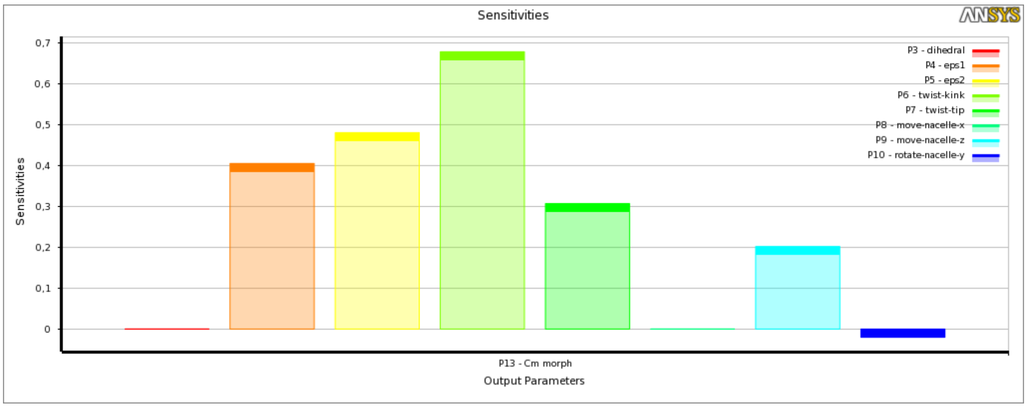

Figure 5.23 - Global sensitivity chart of Cm (fine mesh)

It is very interesting to observe that the Cm coefficient has a similar response in both analyzed cases.

The global sensitivities chart shows the global sensitivities of the output parameters with respect to the input parameters.

Figure 5.24 - Global Sensitivity chart (coarse mesh)

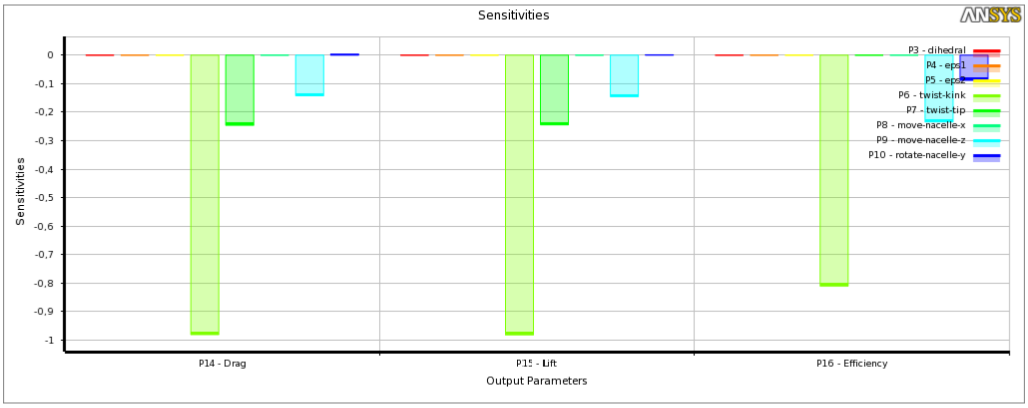

Figure 5.25 - Global Sensitivity chart (fine mesh)

Both global and local sensitivity chart show that the feature which most influences output parameters (*Lift*, *Drag* and *Efficiency*) is the twist at the kink of the wing. Also twist tip affects output values, they both have a negative influence to lift and drag and therefore a negative impact to the lift-to-drag ratio. Moreover, another parameter should be considered, a changing of sweep angle of the outer wing section (from kink to tip) worsens the efficiency given that drag increases with this parameter (see local sensitivity chart). Nacelle displacements have a lower effect than wing parameters, but vertical displacement along Z-axis and rotation around Y-axis of the nacelle appreciably distort efficiency.

For a more thorough analysis, response surface graph of twist angles versus efficiency and other response chart of the most important specifications are shown below. As depicted in Figure 5.26 and Figure 5.27 response surfaces are very similar for coarse and fine mesh.

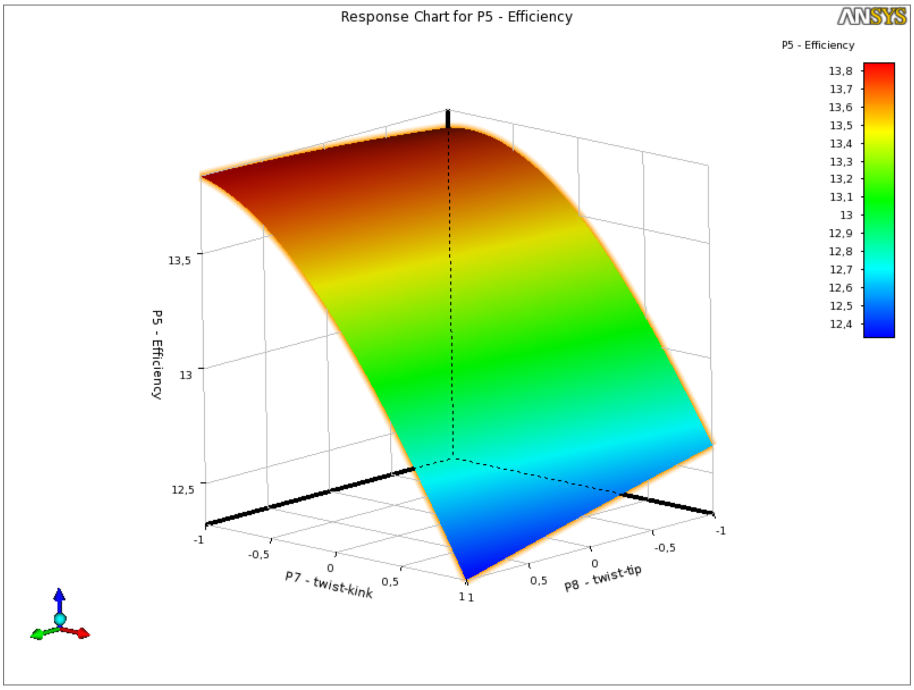

Figure 5.26 – Efficiency vs. twist kink and tip response surface (coarse mesh)

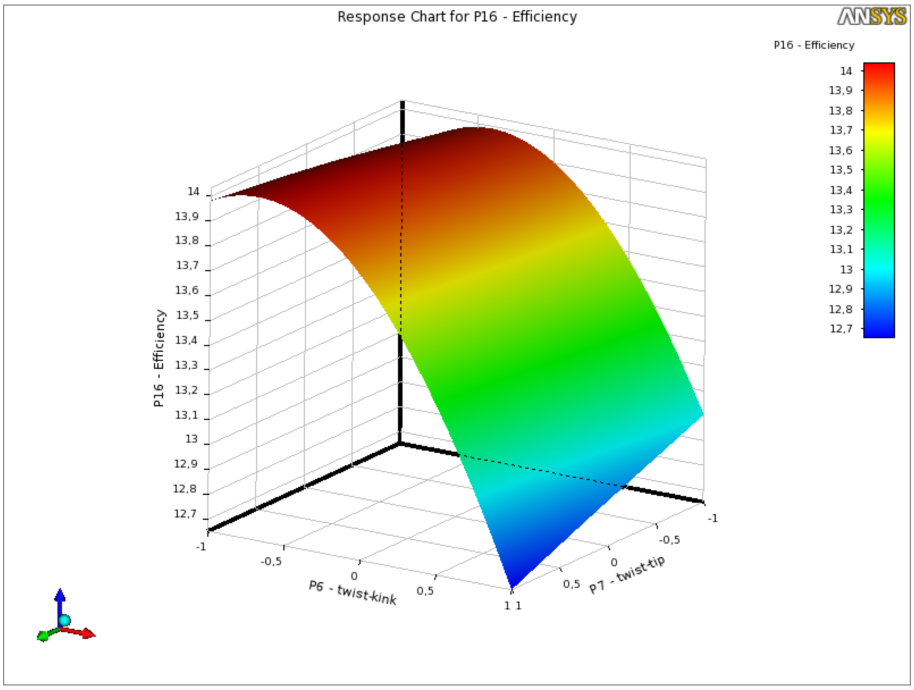

Figure 5.27 - Efficiency vs. twist kink and tip response surface (fine mesh)

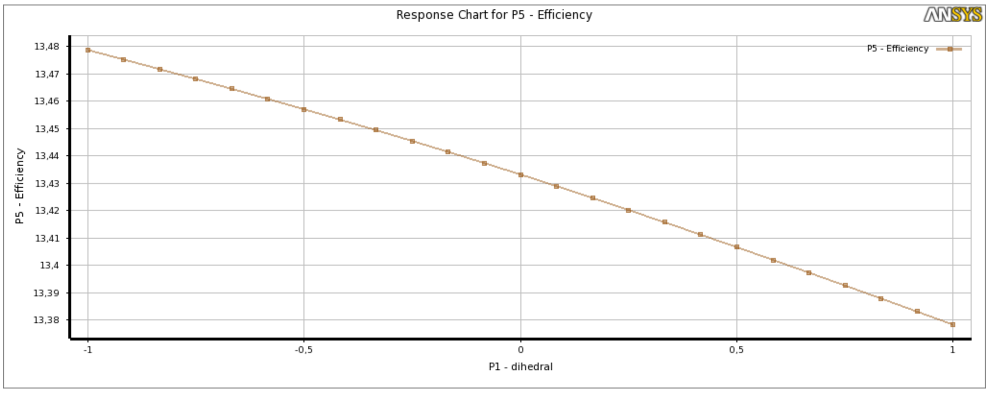

Figure 5.28 - Efficiency vs. dihedral response chart (coarse mesh)

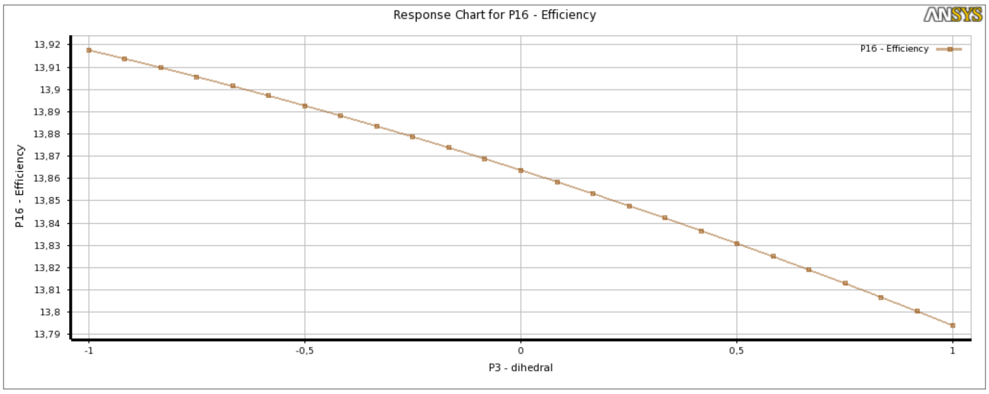

Figure 5.29 - Efficiency vs. dihedral response chart (fine mesh)

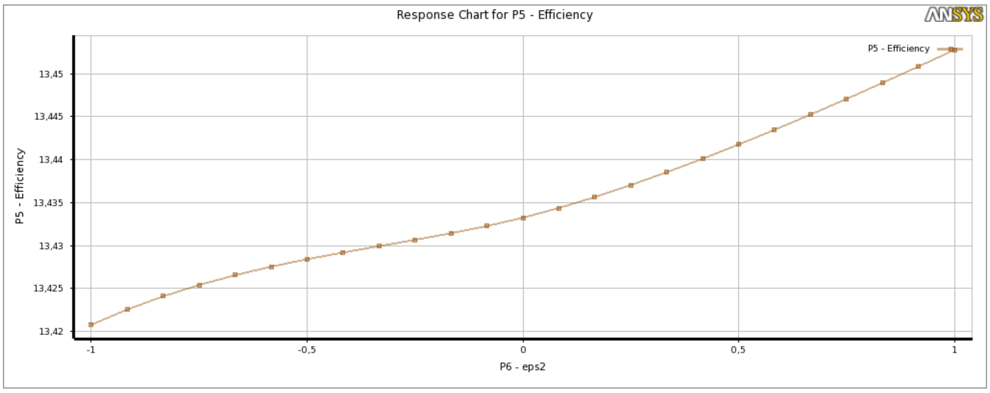

Figure 5.30 – Efficiency vs. eps1 response chart (coarse mesh)

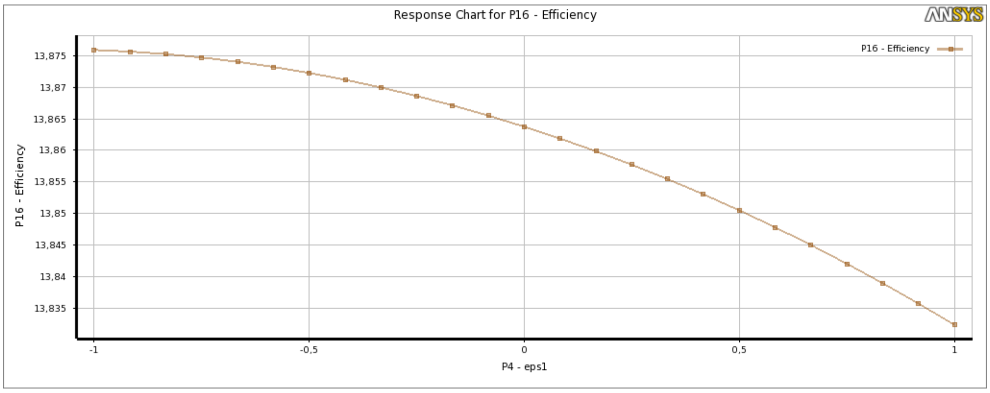

Figure 5.31 – Efficiency vs. eps1 response chart (fine mesh)

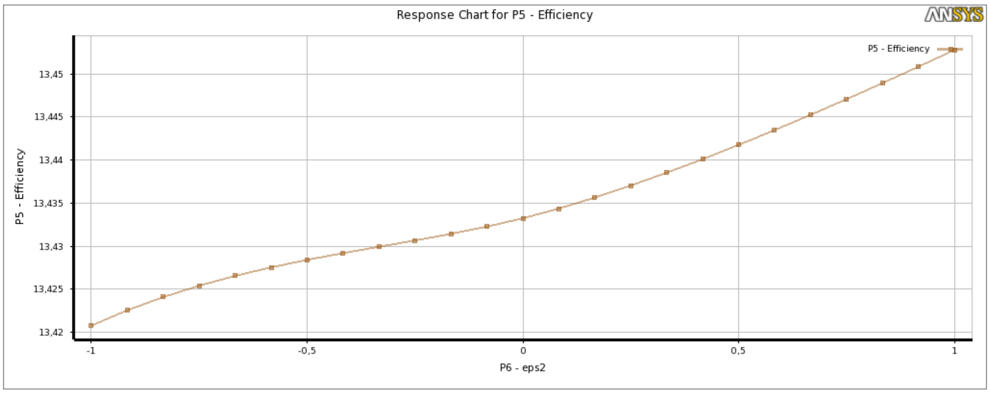

Figure 5.32 - Efficiency vs. eps2 response chart (coarse mesh)

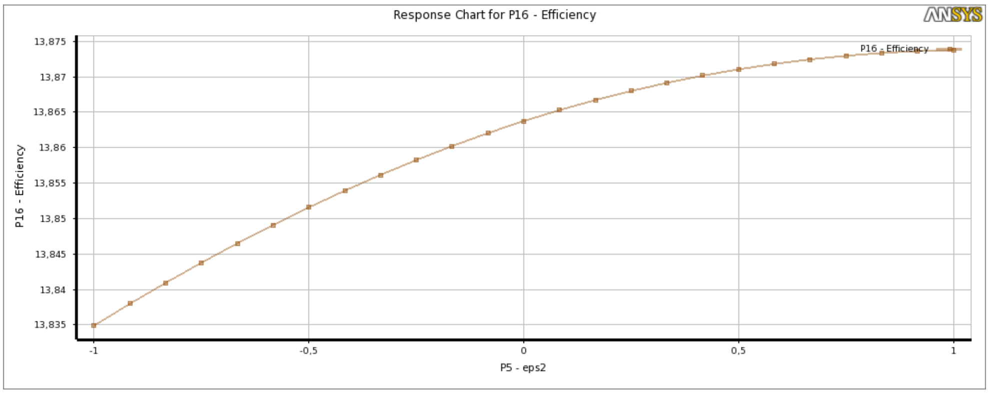

Figure 5.33 – Efficiency vs. eps2 response chart (fine mesh)

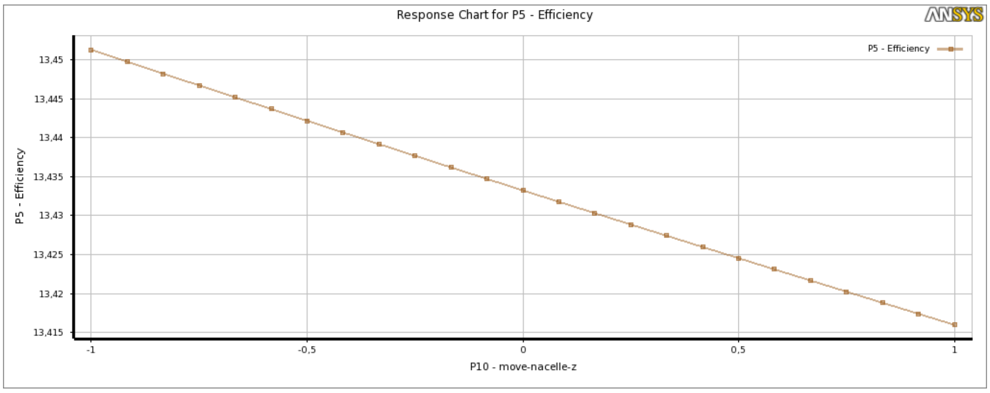

Figure 5.34 – Efficiency vs. z nacelle translation response chart (coarse mesh)

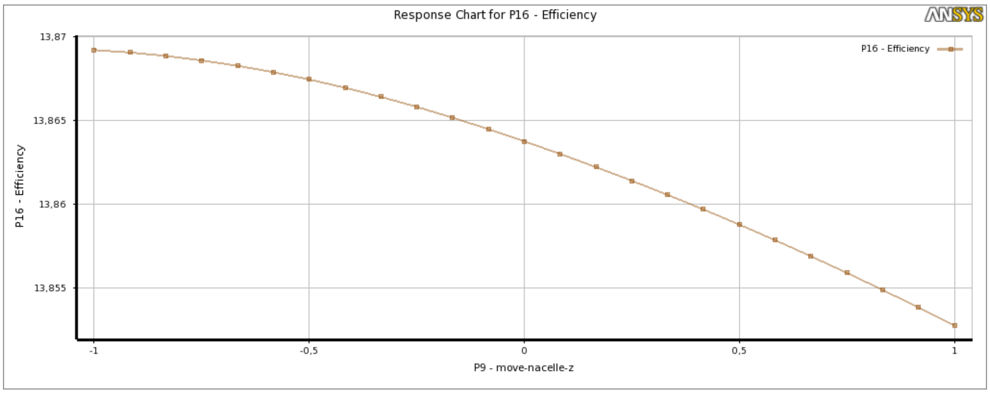

Figure 5.35 – Efficiency vs. z nacelle translation response chart (fine mesh)

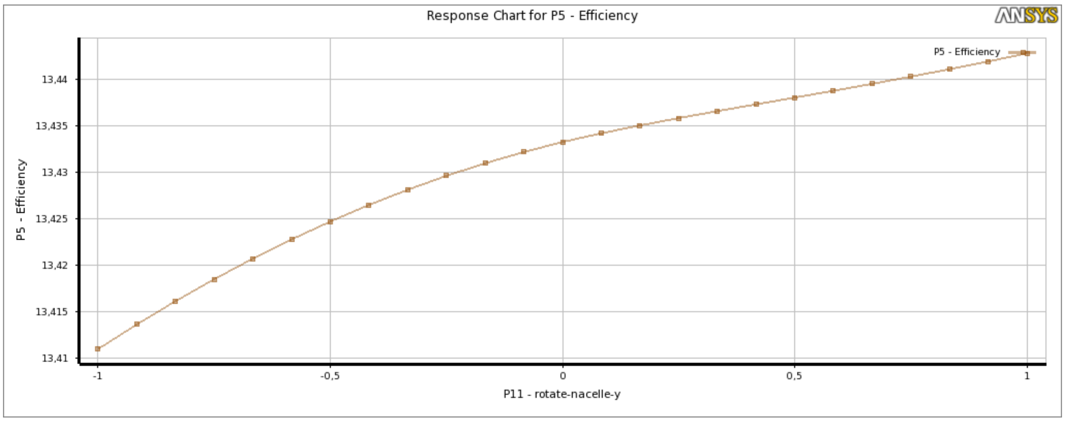

Figure 5.36 - Efficiency vs. y nacelle rotation response chart (coarse mesh)

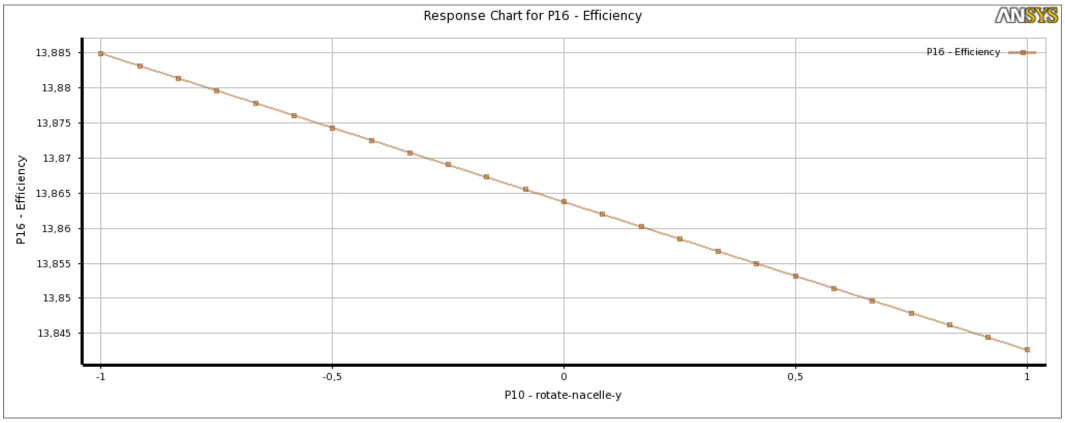

Figure 5.37 - Efficiency vs. y nacelle rotation response chart (fine mesh)

6 RESULTS

The optimization of the aircraft configuration has been accomplished by means of *ANSYS Workbench* using a *Multi-Objective Genetic Algorithm (MOGA)*. The MOGA method is a hybrid variant of the popular *NSGA-II (Non-dominated Sorted Genetic Algorithm-II)* based on controlled elitism concepts.

In a genetic algorithm, a population of candidate solutions to an optimization problem is evolved toward better solutions. Each candidate solution has a set of properties which can be mutated and altered.

The evolution usually starts from a population of randomly generated individuals and it is an iterative process, with the population in each iteration called a generation. In each generation, the fitness of every individual in the population is evaluated; the fitness is usually the value of the objective function in the optimization problem being solved. The more fit individuals are stochastically selected from the current population, and each individual's genome is modified (recombined and possibly randomly mutated) to form a new generation. The new generation of candidate solutions is then used in the next iteration of the algorithm. Commonly, the algorithm terminates when either a maximum number of generations has been produced, or a satisfactory fitness level has been reached for the population.

In the following table, three possible candidates for the optimization are presented. They are referred to the fine mesh since it has default coefficients values closer to the wind tunnel model than the coarse one.

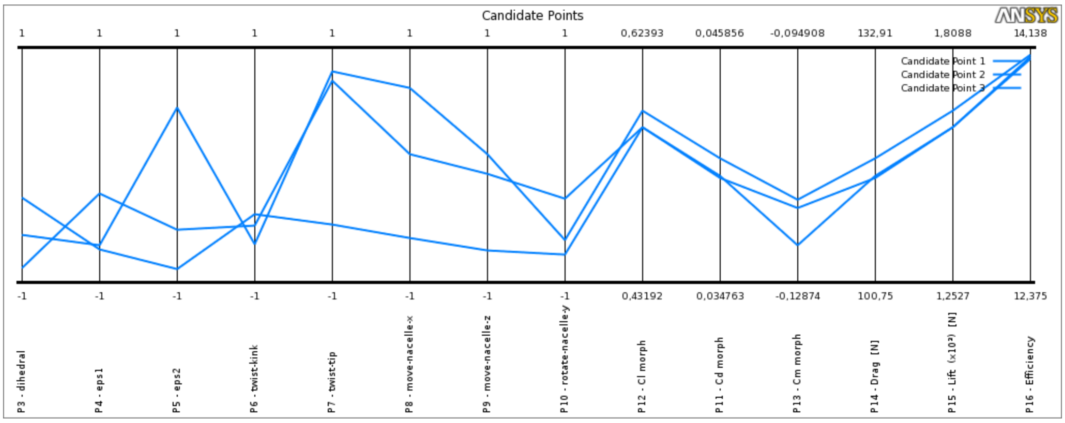

Figure 6.1 – Input and output values of design point, fine mesh

Table 6.1 – Candidate points and baseline input values, fine mesh

DESIGN POINT	dihedral	eps1	eps2	twist-kink	twist-tip	move-nacelle-x	move-nacelle-z	rotate-nacelle-y
Baseline	0	0	0	0	0	0	0	0
Candidate A	-0,81	0,135	-0,916	0,690	-0,378	0,646	0,395	0,0689
Candidate B	-0,874	-0,397	-0,688	0,706	0,446	-0,086	0,264	0,881
Candidate C	-0,068	-0,389	-0,982	0,521	-0,662	0,162	0,37262	0,137

Table 6.2 - Candidate points and baseline output values, fine mesh

DESIGN POINT	Cd	Cl	Cm	Drag (N)	Lift (N)	Efficiency	**Δ-Efficiency**
Baseline	0,0381	0,528	-0,114	110,42	1530,9	**13,86**	---
Candidate A	0,0397	0,559	-0,118	115,20	1621,2	**14,07**	**1,56%**
Candidate B	0,0407	0,573	-0,117	117,86	1660,5	**14,09**	**1,67%**
Candidate C	0,0398	0,560	-0,123	115,39	1621,9	**14,06**	**1,44%**

Candidate B represents the best configuration which can be obtained; it is important to notice that all candidate have a higher lift compared to the baseline value and drag is quite increased. Even though all candidates have a similar efficiency, candidate B should be preferred because it has the highest lift value. It is also important to remind that baseline values for both meshes have been compared with the same ones of the wind tunnel experimentation.

A valid method to evaluate the goodnes of the present work is to compare the values of the pressure coefficient along the wingspan. Eight section of the wing have been studied and compared with the results from wind tunnel experiment.

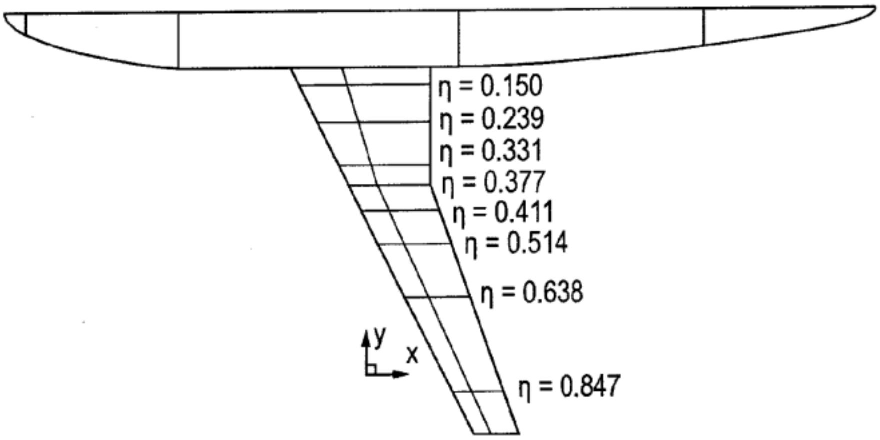

Figure 6.2 – Different η along the wingspan

From Figure 6.3 to Figure 6.10 plots of the pressure coefficient Cp with experimental data and baseline are presented. The main difference between two kind of meshes can be noticed at η=0,331 where the nacelle is placed; in that point fine mesh has a bad quality, whereas the coarse mesh keeps a good quality. A little discrepancy should also be detected near the root of the wing (η=0,15) at the leading edge where Cp values of meshes are quite bigger than Cp from wind tunnel data. This phenomenon is probably due to the fairing configuration near the wing, in fact, in the following *Workshops,* this feature has been changed to avoid flow separation in the nearness of the root of the wing.

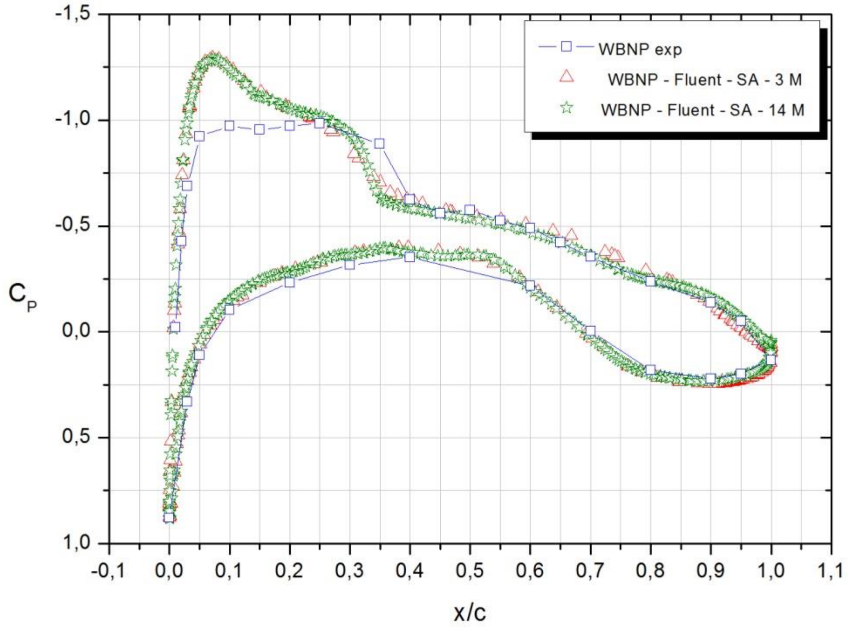

Figure 6.3 – Cp at η=0,15, wind tunnel data, coarse and fine mesh baseline

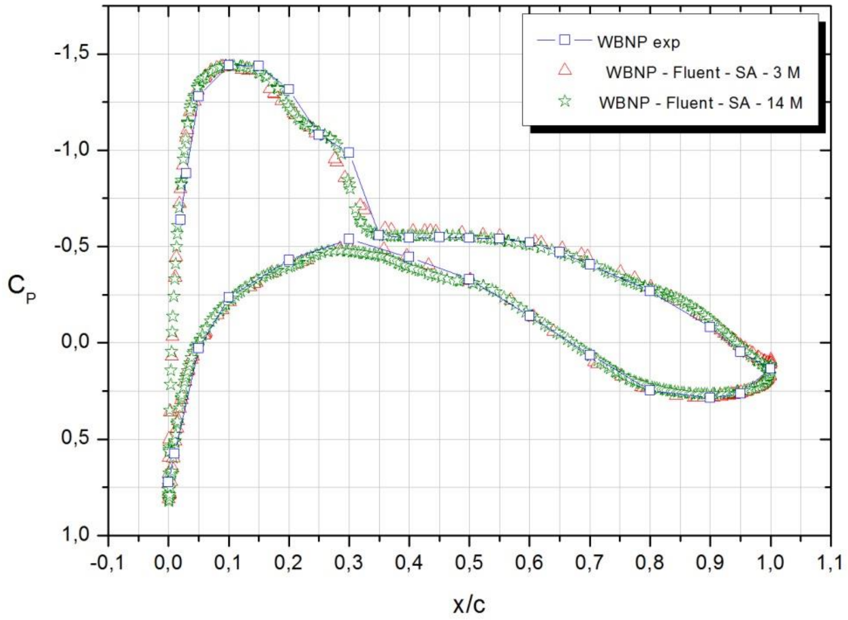

Figure 6.4 – Cp at η=0,239, wind tunnel data, coarse and fine mesh baseline

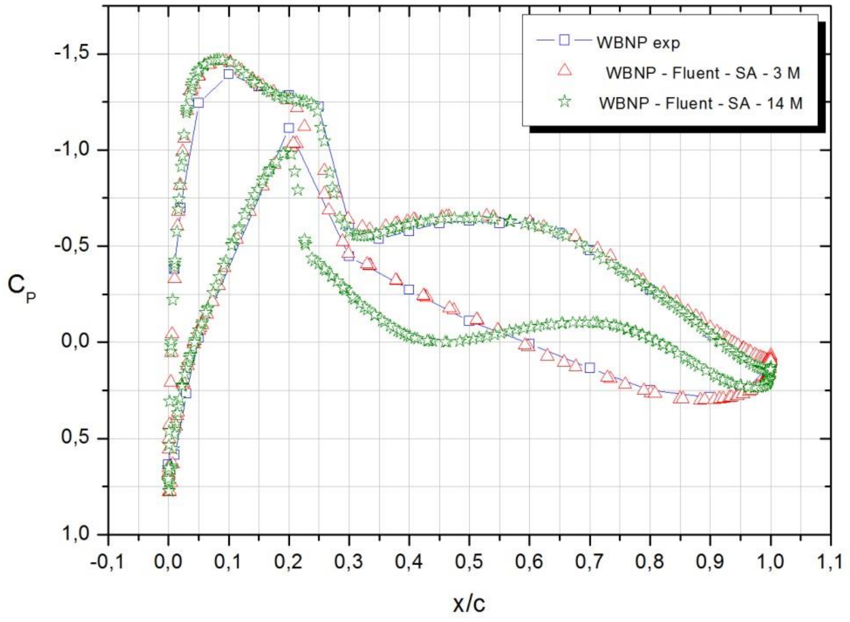

Figure 6.5 – Cp at η=0,331, wind tunnel data, coarse and fine mesh baseline

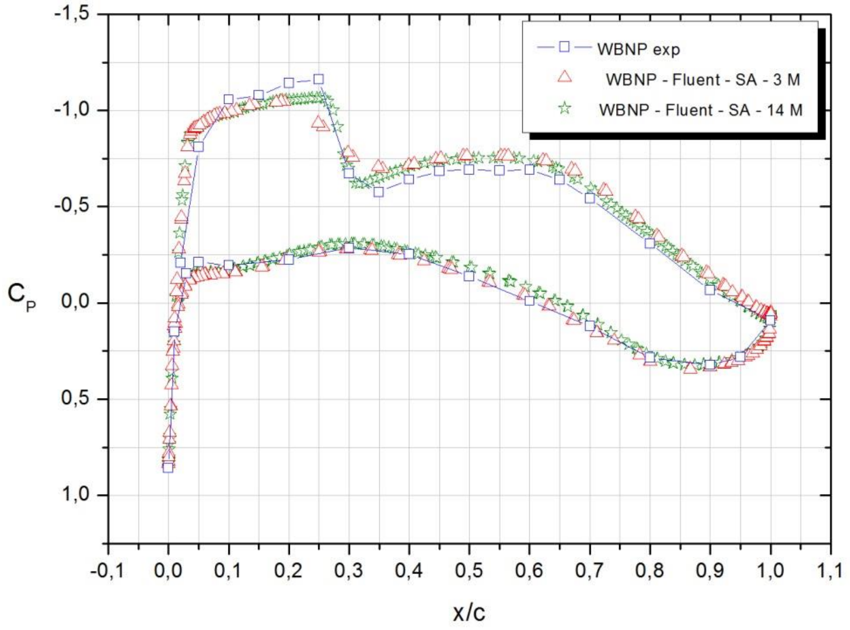

Figure 6.6 – Cp at η=0,377, wind tunnel data, coarse and fine mesh baseline

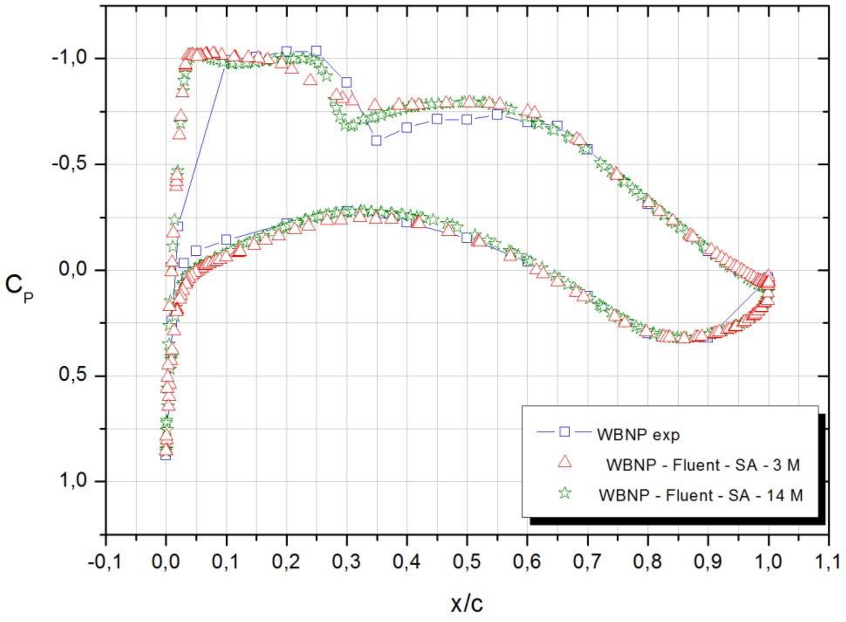

Figure 6.7 – Cp at η=0,411, wind tunnel data, coarse and fine mesh baseline

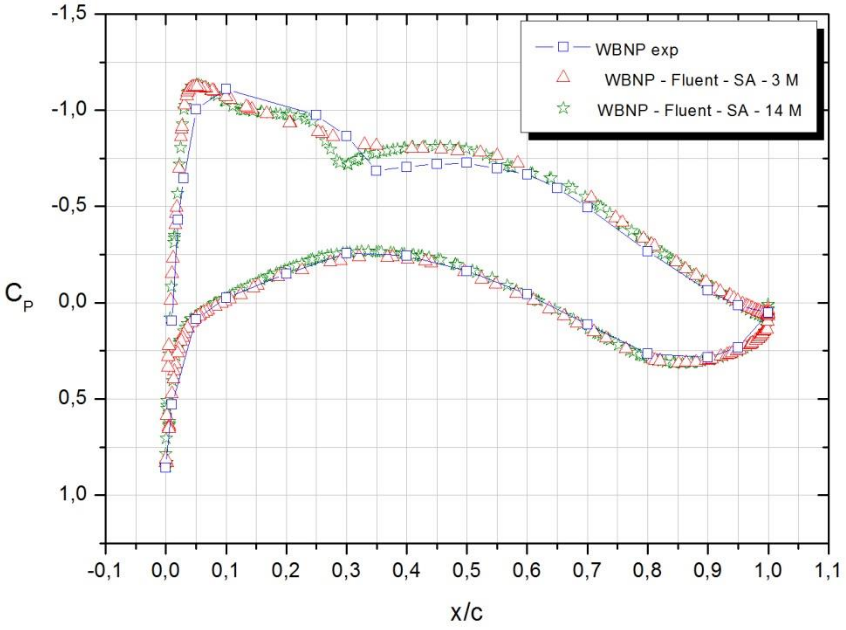

Figure 6.8 – Cp at η=0,514, wind tunnel data, coarse and fine mesh baseline

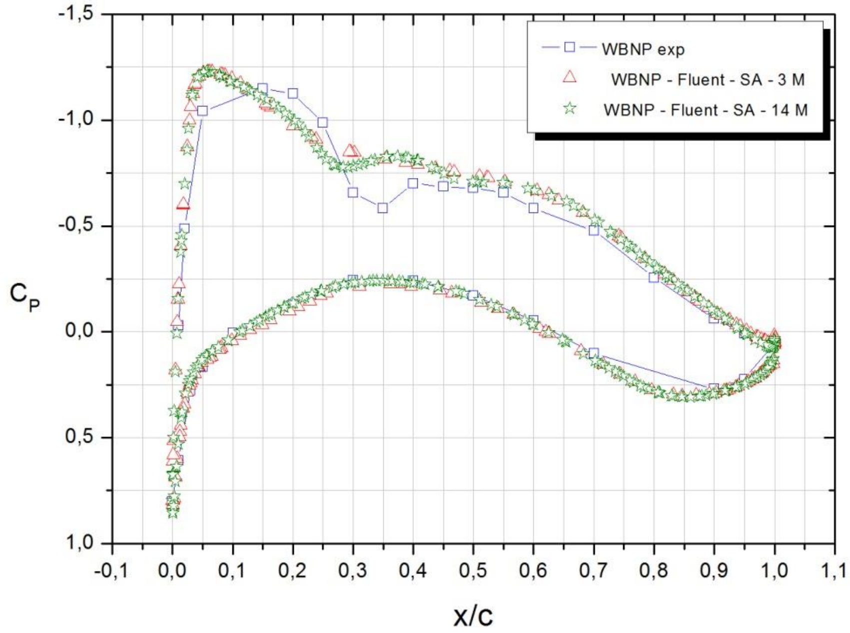

Figure 6.9 – Cp at η=0,638, wind tunnel data, coarse and fine mesh baseline

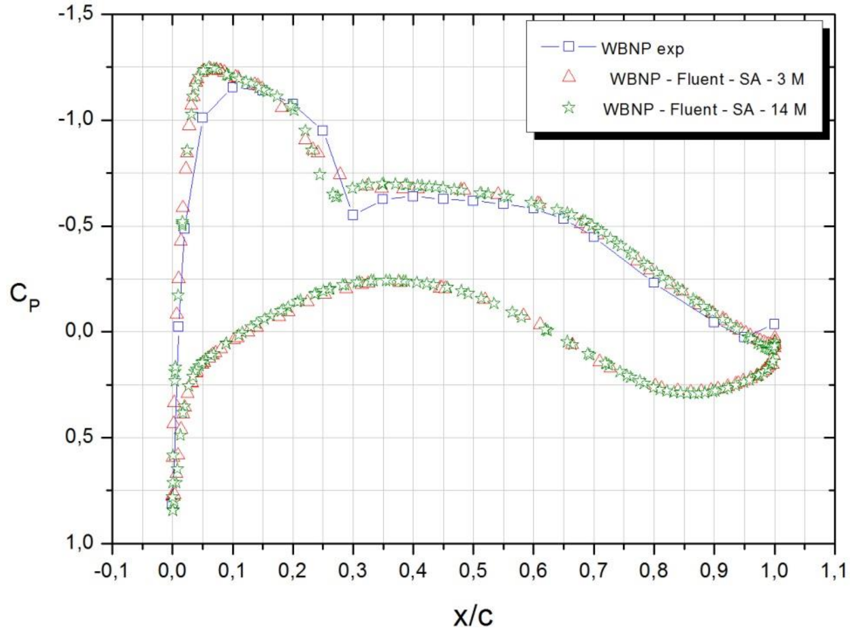

Figure 6.10 – Cp at η=0,847, wind tunnel data, coarse and fine mesh baseline

The following graphs show Cp values along the wingspan, three curves are presented, they are referred to wind tunnel data, baseline results and values after optimization for fine mesh (14 million of cells). As depicted in graphs, Cp values, which are related to the optimized configuration, decrease as you move from root to tip on the upper surface of the wing. This phenomenon proves that lift is really increased in the optimized.

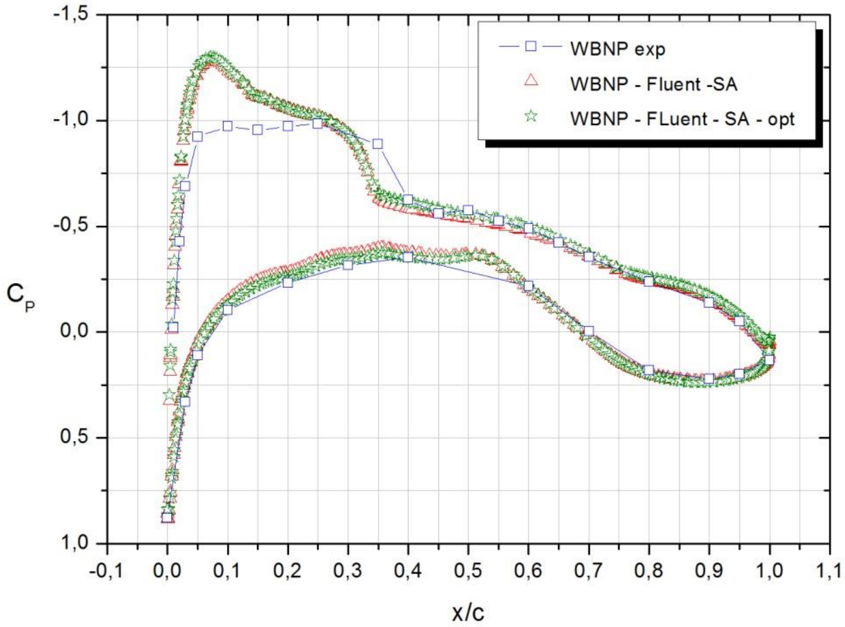

Figure 6.11 – Cp at η=0,15, fine mesh

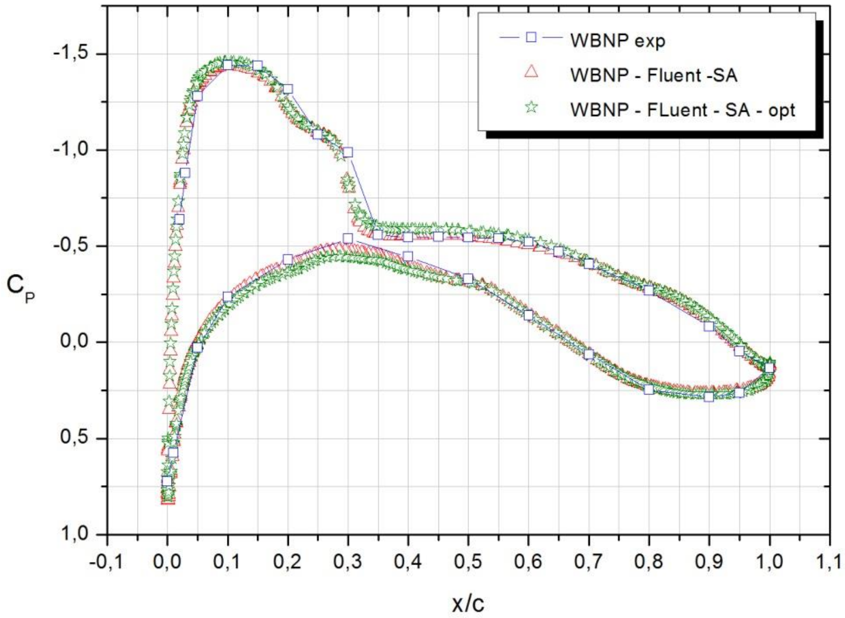

Figure 6.12 – Cp at η=0,239, fine mesh

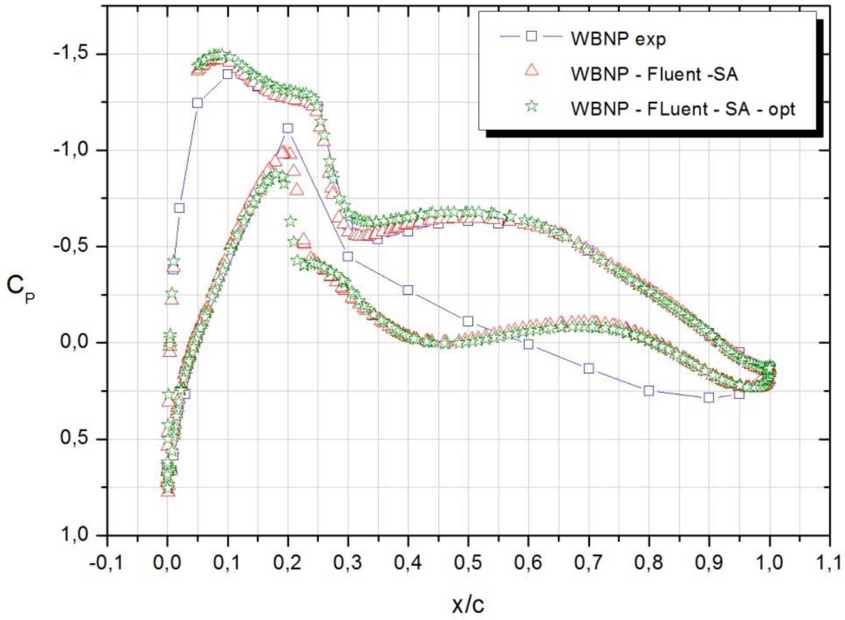

Figure 6.13 – Cp at η=0,331, fine mesh

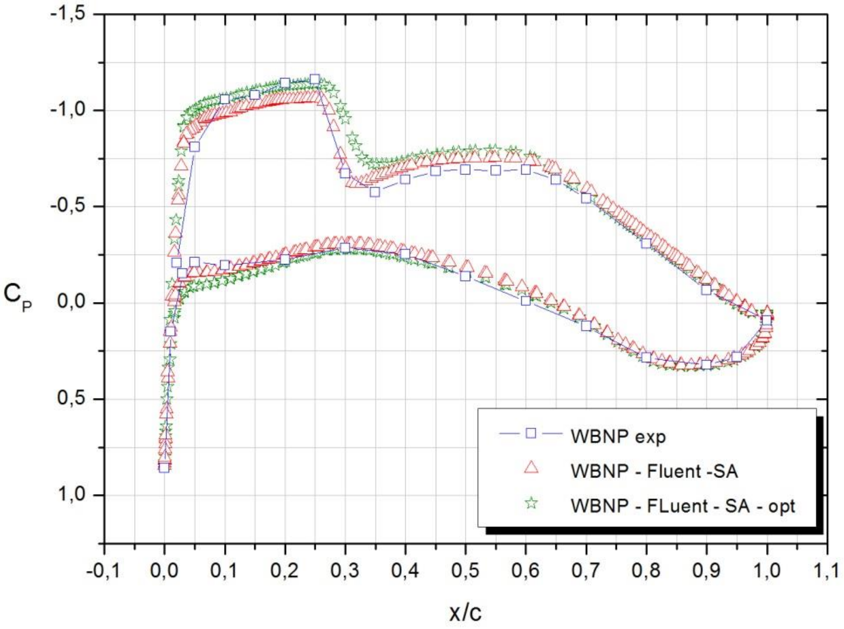

Figure 6.14 – Cp at η=0,377, fine mesh

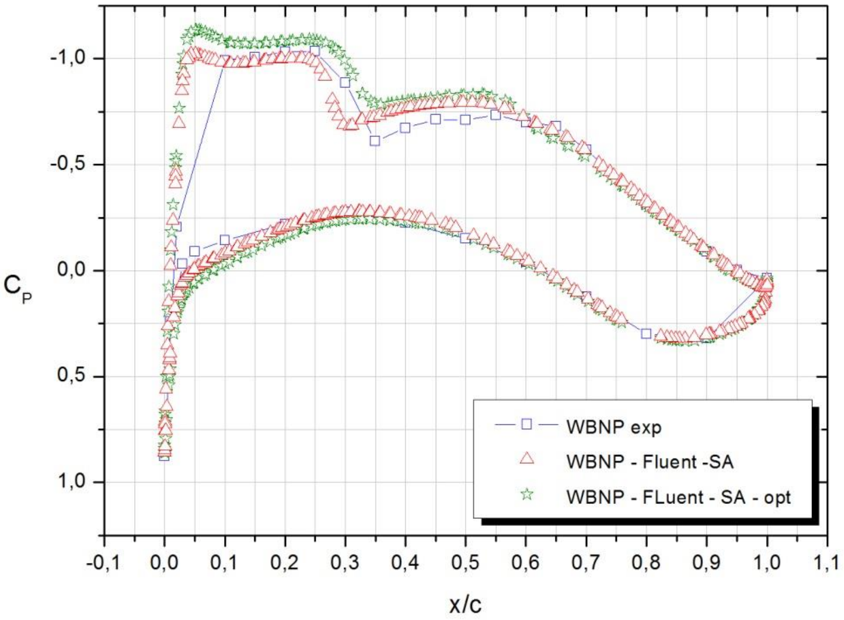

Figure 6.15 – Cp at η=0,411, fine mesh

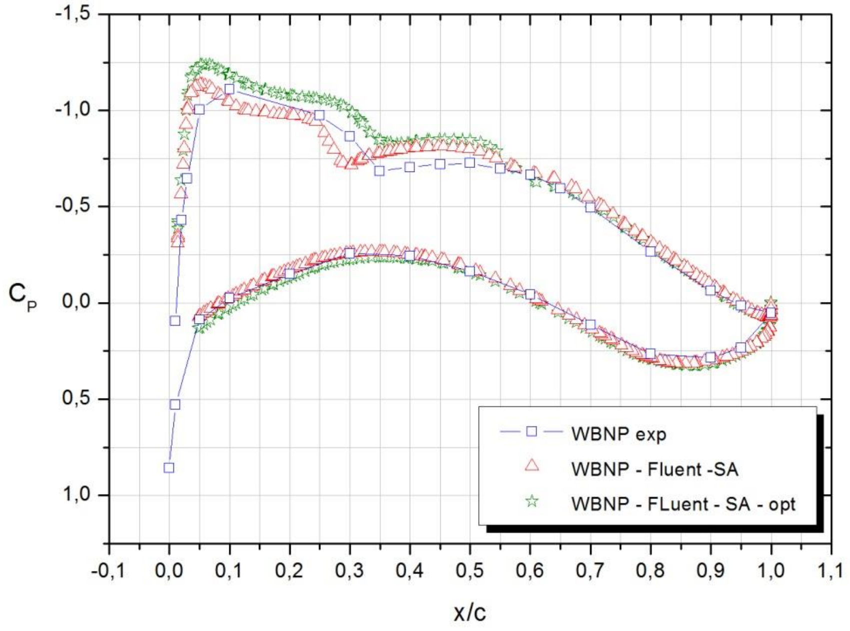

Figure 6.16 – Cp at η=0,514, fine mesh

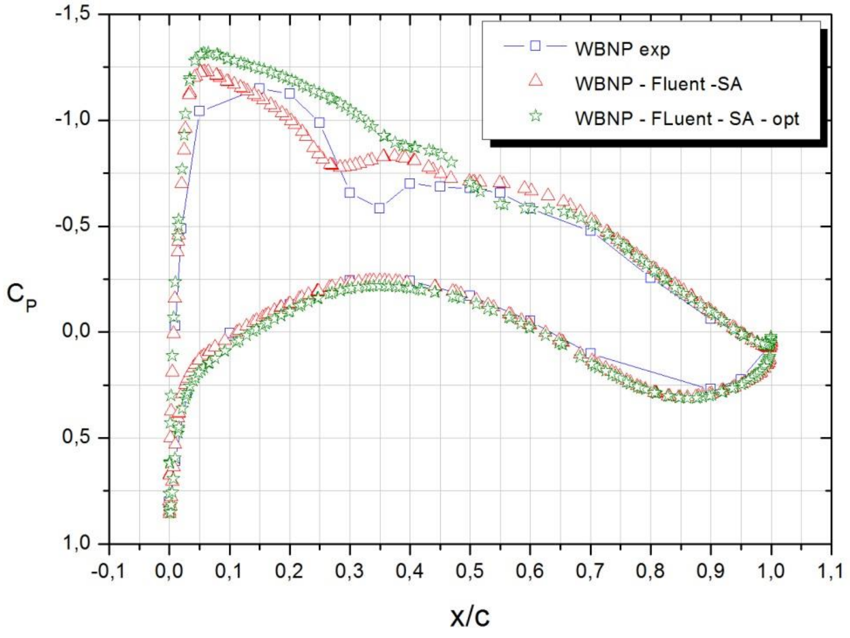

Figure 6.17 – Cp at η=0,638, fine mesh

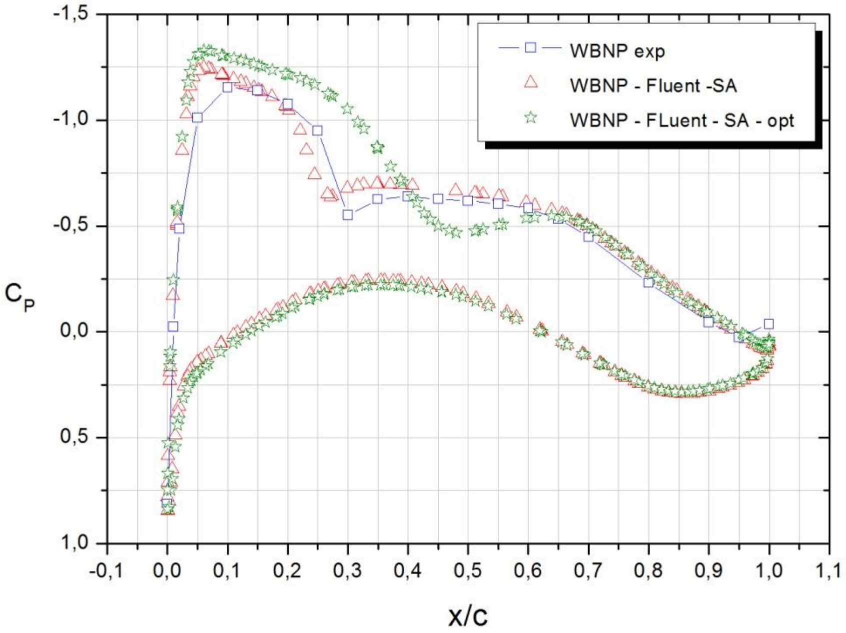

Figure 6.18 – Cp at η=0,847, fine mesh

To better understand pressure distribution acting on the wing, two contour plots about total pressure are shown below. You can notice that the optimal arrangement has a lower pressure on the upper surface of the wing than the baseline and its distribution is smoother. The same effect can be noticed in Cp plots already presented and it appears mainly on the outer section of the wing because, moving gradually from root to tip, nodal displacements become bigger.

It is remembered that pressure formula for a compressible fluid is:

$$\boldsymbol{p_0 = p(1 + \frac{k-1}{2} M^2)^{k/_{k-1}}} \qquad 6.1$$

Where:

p_0 is the total pressure

p is the static pressure

M is the Mach number

$k = c_p/c_v$

Also operating pressure p_{op} (1 atm as default value) is considered in *ANSYS Fluent,* so previous formula becomes the following:

$$\frac{p_0'+p_{op}}{p'+p_{op}} = p\left(1+\frac{k-1}{2}M^2\right)^{k/_{k-1}} \tag{6.2}$$

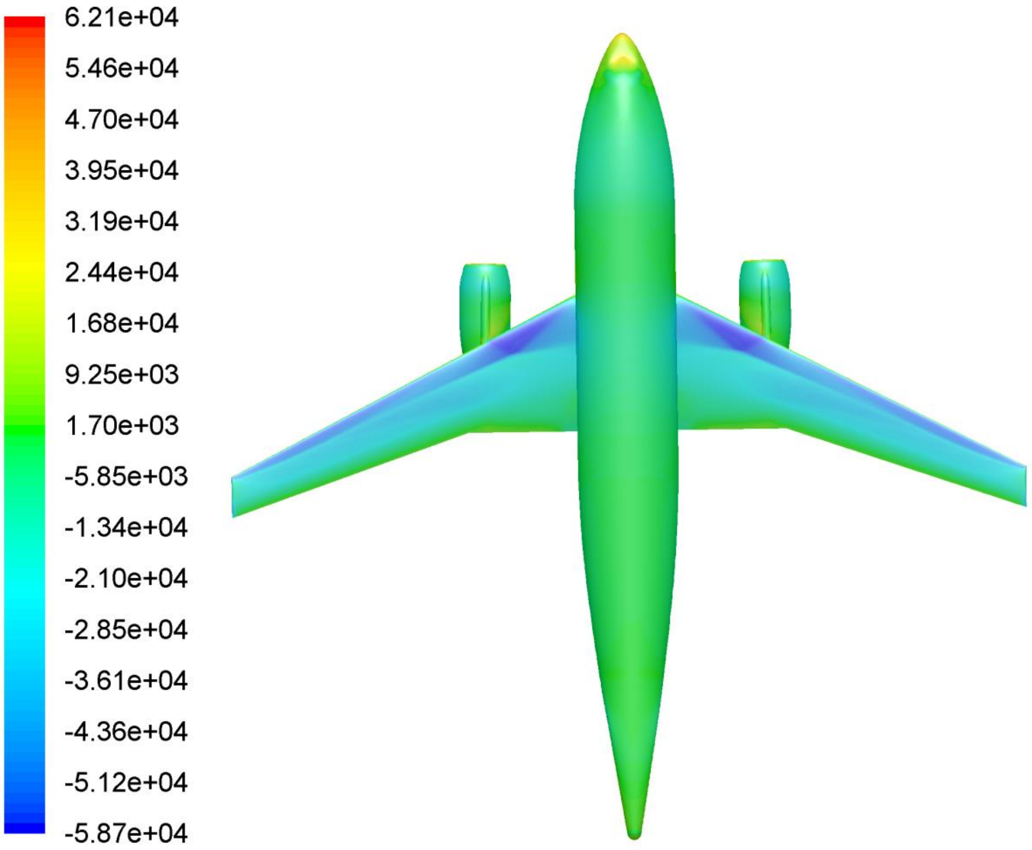

Figure 6.19 – Total pressure distribution on the model in the baseline configuration (Pa)

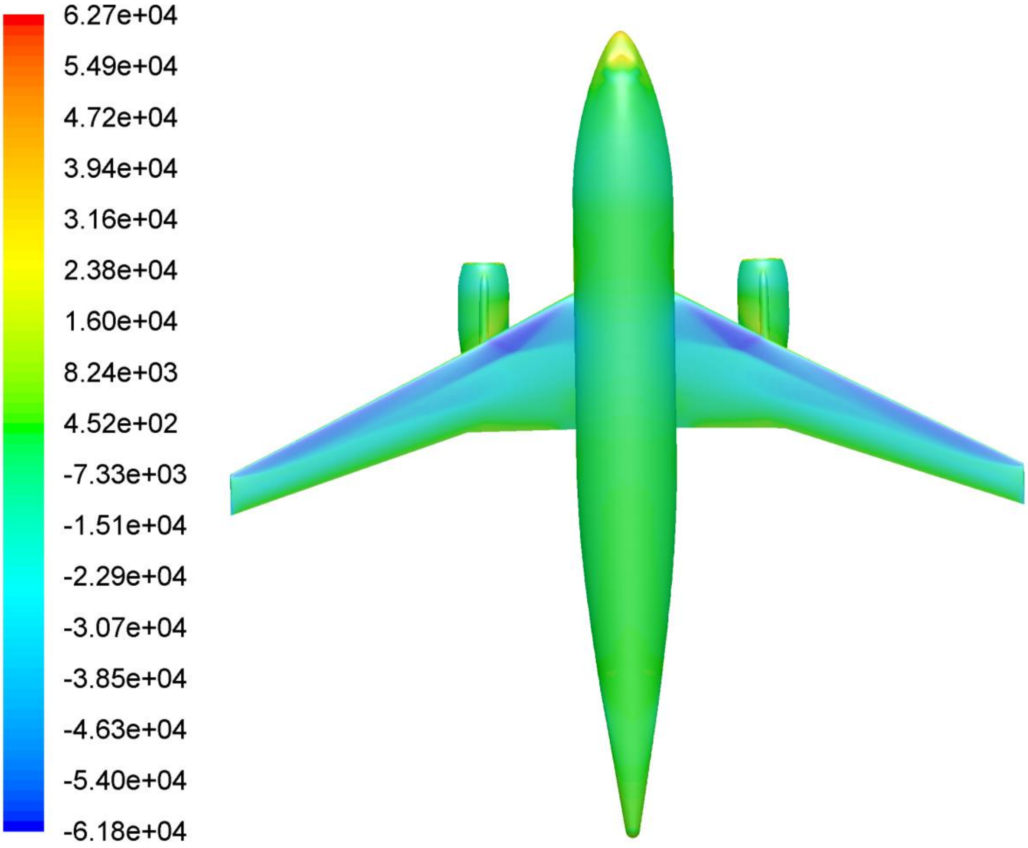

Figure 6.20 - Total pressure distribution on the model in the optimized configuration (Pa)

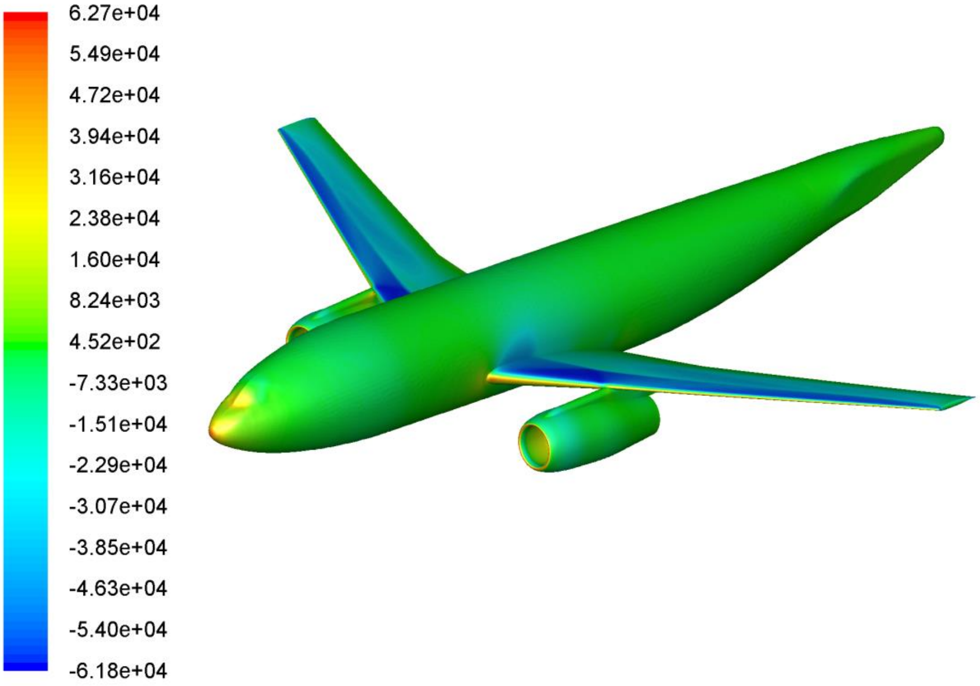

Figure 6.21 - Total pressure distribution on the model in the baseline configuration (Pa)

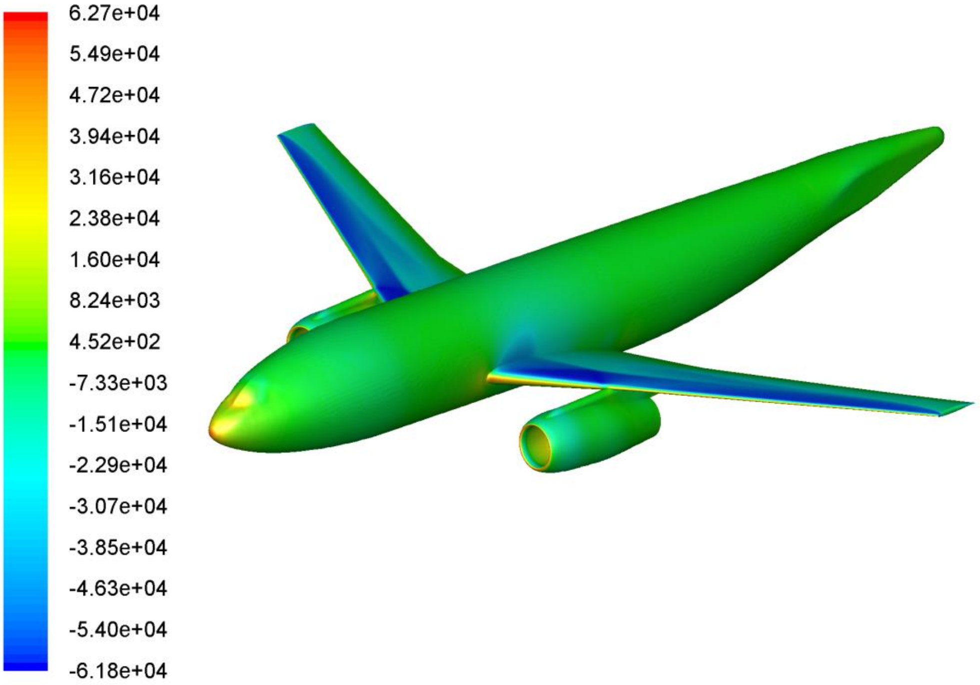

Figure 6.22 - Total pressure distribution on the model in the optimized configuration (Pa)

7 CONCLUSIONS AND FUTURE WORK

In this thesis an aircraft design optimization by means of *Radial Basis Function* has been presented. The aim of this research consisted in finding a better configuration of DLR-F6 through the study of eight parameters of wing and nacelle such as dihedral angle, sweep angle and twist of the wing and two rigid translations and one rotation of the nacelle.

Thesis workflow was composed by several steps and it was applied to two meshes, a coarse mesh (3 million of cells) and a fine mesh (14 million of cells).
First step was simulating with *ANSYS Fluent* cruise condition of the aircraft and comparing results with the experimental values from wind tunnel tests at the *ONERA* facility.
Once that baseline results have been validated, mesh morphing has been applied to the two grids using the same *RBF* setup in order to obtain parametric meshes.
Last step involved in a design exploration, *DOE* permitted to find the best combination of the above-mentioned specifications improving efficiency.

The present workflow has shown to be useful for shape optimization and it can be used for a wide range of fluid dynamics cases.

Radial Basis Functions have proven to be a solid tool for mesh morphing application, granting both speed and quality and allowing to define the displacement of the interested nodes only. *RBF-Morph* has demonstrated to be a *grid independent* add-on for *ANSYS Fluent* and its integration into design optimization workflow seems feasible.

Future developments and researches could lead to a study of meshes with better quality, other parameters could be studied such as angle of incidence. Wing shape could be modified acting directly on the airfoil section in order to achieve a better behaviour of the wing. The more difficult and complicated design of experiment and mesh refinement are, the more computational performances are requested, so future works could be processed by means of *HPC (High Performance Computing).* For this reason some trial of remote computing have been done on a *Linux* cluster. This methodology is quite different than the used one because *ANSYS Workbench* can’t be used on *Linux* cluster, so the whole workflow have to be completely done using text commands, without a graphic interface.

BIBLIOGRAPHY

[1] Inc. Ansys. *Ansys FLUENT Theory guide*. Ver. 14.0. November. 201

[2] Inc. Ansys. *Ansys FLUENT Workbench user guide*. Ver. 14.5. October 2012.

[3] Inc. Ansys. *Ansys FLUENT Design Exploration user guide*. Ver. 14.5. October 2012.

[4] Inc. Ansys. *RBF-Morph user guide.* Ver. 1.3. July 2011

[5] Inc. Ansys. *RBF-Morph Tutorial 10:Aircraft.* Ver. 1.3. January 2012

[6] M. Rakowitz. *2nd AIAA Drag Prediction Workshop DLR-F6 Geometry & Issues.* 2003

[7] J.L.Godard. *F6 model tests in the ONERA S2MA wind-tunnel*. 2003

[8] T. Scheiddegger, G. Stuckert. *2nd AIAA CFD Drag Prediction Workshop*. 2003

[9] Ochi, E. Shima. *A drag prediction validation study for aircraft aerodynamic Analysis.* 2004

[10] M. E. Biancolini , U. Cella *Optimization of wing efficiency vs. sweep angles using v mesh morphing.* 2012

[11] S.Wallin. *Description of test case: AC02 DLR F6*. 2010

[12] R. M. Kulfan. *Prediction of nacelle aerodynamic interference effects at low supersonic mach numbers. 1980*

[13] O. Brodersen, A. Stürmer. *Drag prediction of engine–airframe interference effects using unstructured navier–stokes calculations.* 2001

[14] H. K. Versteeg, W. Malalasekera. *An Introduction to Computational Fluid Dynamics*. Longman Scientific & Technical. New York. 1995

[15] B. John, C. Baxter. *The interpolation theory of radial basis functions. 1992*

[16] S. R. Allmaras, F. T. Johnson, P. R. Spalart. *Modifications and Clarifications for the Implementation of the Spalart-Allmaras Turbulence Model.* 2012

[17] B. Husslage, G. Rennen, E. R. van Dam, D. den Hertog. *Space-filling latin hypercube designs for computer experiments.* 2006

[18] Konak, D. W. Coit, A. E. Smith. *Multi-objective optimization using genetic algorithms* 2006

[19] R.Verzicco . *Appunti di fluidodinamica*. 2006

[20] R.Verzicco. *Appunti di Turbolenza.* 2006

[21] R.Barboni. *Fondamenti di aerospaziale.* 2003

[22] G.Graziani. *Aerodinamica.* 2ª Edizione Casa editrice Università La Sapienza. Roma.2008

[23] Wilcox D.C, *Turbulence modeling for CFD.* 1993

[24] Dhanalakshmi Srinivasan college of Engineering & Technology by C. Amarnath R.Chandramohan *Aircraft " Wing Twist".* 2012

[25] Tesi di laurea in ing. Meccanica, Dariva Jacopo, *Ottimizzazione aerodinamica mediante mesh morphing: il caso del DLR-F6*

[26] http://history.nasa.gov

[27] http://adg.stanford.edu/aa241/propulsion/engineplacement.html

[28] http://www.cfd-online.com

Acknowledgements

Perché scrivere una tesi completamente in inglese per finire poi con i ringraziamenti in italiano?

La risposta è semplice ma non banale.
Perché le persone alle quali devo esprimere tutta la mia riconoscenza e gratitudine sono italiane e non tutte parlano bene l'inglese. In questo modo sono sicuro che ognuno potrà apprezzare quanto scritto e soprattutto capirlo.

In primis mi sembra doveroso dover ringraziare il mio relatore, l'ing. Marco Evangelos Biancolini, che mi ha permesso di svolgere questo lavoro di tesi. Ringrazio anche l'ing. , ed ormai amico, Corrado Groth che con la sua pazienza e la sua disponibilità mi ha seguito in ogni dettaglio del mio lavoro. Altra persona importante da ringraziare che ha contribuito molto in questo percorso è l'ing. Emiliano Costa.

Le singole persone che più di tutti meritano che questo lavoro sia loro dedicato sono certamente i miei genitori. A loro va tutta la mia stima, il mio rispetto e la mia riconoscenza, nonostante le incomprensioni che inevitabilmente si sono presentate nel corso degli anni. Loro mi hanno sempre sostenuto sia economicamente che psicologicamente dimostrando sempre piena fiducia nelle mie scelte di vita. Spero di riuscire ad essere con i miei figli, se mai ne avrò, almeno la metà di ciò che sono stati loro per me.

Altra persona molto importante della mia vita è lei, Barbara Rossi. Non smetterò mai di ringraziarla per tutto il sostegno, l'amore che mi ha sempre dato e soprattutto per la pazienza dimostrata durante i lunghi periodi di studio senza vederci. Lei mi ha accompagnato in tutta la mia crescita universitaria e non solo. Grazie di esistere.

Un sentito grazie va ai miei nonni ai quali ho dedicato la mia prima tesi, mi dispiace ma questa volta tocca a mamma e a papà. Grazie a mia zia Daniela, che con le sue attività di *coaching* e la *PNL* mi ha fatto capire che è possibile superare ogni ostacolo, basta che siamo noi stessi a volerlo veramente.

Un pensiero particolare va a tutti i miei compagni di corso, siete troppi per essere nominati, con i quali mi sono spesso confrontato e ho condiviso gioie e dolori universitari. Loro, più di tutti, possono comprendere il mio grado di soddisfazione in questo momento.

Infine, ultimo, ma non per importanza, vorrei ringraziare mio fratello Paolo, per il quale spero di essere sempre un buon modello da seguire, continua a crescere così che vai bene.